Textural characterization, major and volatile element quantification and Ar–Ar systematics of spherulites in the Rocche Rosse obsidian flow, Lipari, Aeolian Islands: a temperature continuum growth model

P. L. Clay, B. O'Driscoll, R. Gertisser, H. Busemann, S. C. Sherlock & S. P. Kelley

Contributions to Mineralogy and Petrology

ISSN 0010-7999
Volume 165
Number 2

Contrib Mineral Petrol (2013)
165:373-395
DOI 10.1007/s00410-012-0813-x

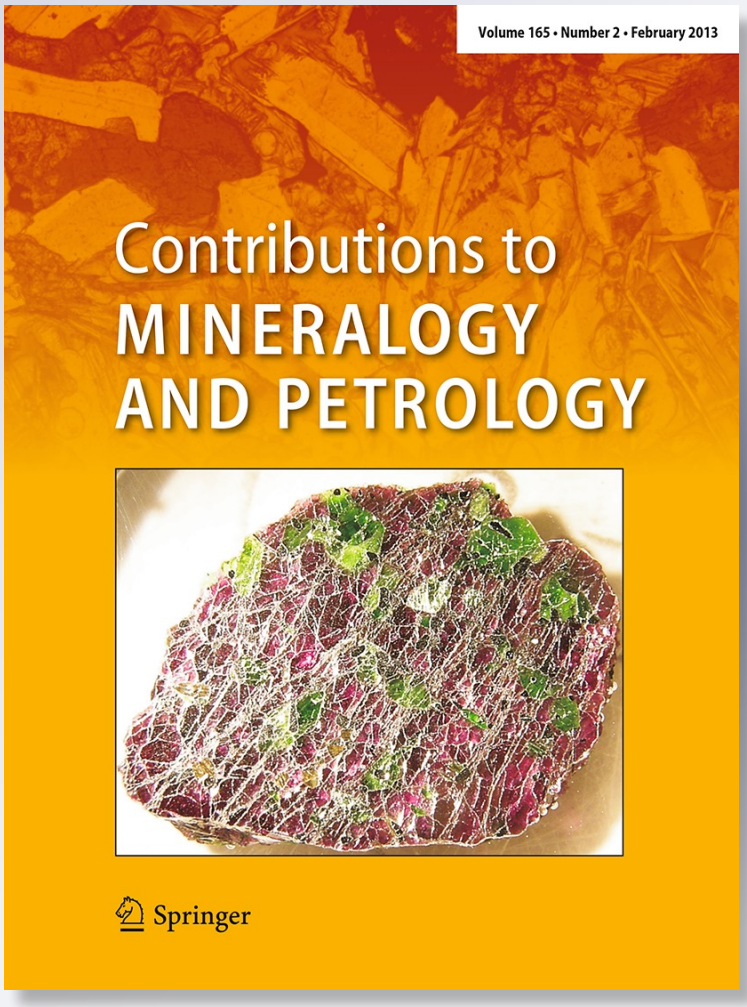

Springer

Contrib Mineral Petrol (2013) 165:373–395
DOI 10.1007/s00410-012-0813-x

ORIGINAL PAPER

Textural characterization, major and volatile element quantification and Ar–Ar systematics of spherulites in the Rocche Rosse obsidian flow, Lipari, Aeolian Islands: a temperature continuum growth model

P. L. Clay · B. O'Driscoll · R. Gertisser · H. Busemann · S. C. Sherlock · S. P. Kelley

Received: 1 April 2012 / Accepted: 10 September 2012 / Published online: 19 October 2012

Abstract Spherulitic textures in the Rocche Rosse obsidian flow (Lipari, Aeolian Islands, Italy) have been characterized through petrographic, crystal size distribution (CSD) and in situ major and volatile elemental analyses to assess the mode, temperature and timescales of spherulite formation. Bulk glass chemistry and spherulite chemistry analyzed along transects across the spherulite growth front/glass boundary reveal major-oxide and volatile (H_2O, CO_2, F, Cl and S) chemical variations and heterogeneities at a $\leq$5 μm scale. Numerous bulk volatile data in non-vesicular glass (spatially removed from spherulitic textures) reveal homogenous distributions of volatile concentrations: H_2O (0.089 ± 0.012 wt%), F (950 ± 40 ppm) and Cl (4,100 ± 330 ppm), with CO_2 and S consistently below detection limits suggesting either complete degassing of these volatiles or an originally volatile-poor melt. Volatile concentrations across the spherulite boundary and within the spherulitic textures are highly variable. These observations are consistent with diffusive expulsion of volatiles into melt, leaving a volatile-poor rim advancing ahead of anhydrous crystallite growth, which is envisaged to have had a pronounced effect on spherulite crystallization dynamics. Argon concentrations dissolved in the glass and spherulites differ by a factor of ~20, with Ar sequestered preferentially in the glass phase. Petrographic observation, CSD analysis, volatile and Ar data as well as diffusion modeling support continuous spherulite nucleation and growth starting at magmatic (emplacement) temperatures of ~790–825 °C and progressing through the glass transition temperature range (T_g ~ 750–620 °C), being further modified in the solid state. We propose that nucleation and growth rate are isothermally constant, but vary between differing stages of spherulite growth with continued cooling from magmatic temperatures, such that there is an evolution from a high to a low rate of crystallization and low to high crystal nucleation. Based on the diffusion of H_2O across these temperature ranges (~800–300 °C), timescales of spherulite crystallization occur on a timescale of ~4 days with further modification up to ~400 years (growth is prohibitively slow <400 °C and would become diffusion reliant). Selective deformation of spherulites supports a down-temperature continuum of spherulite formation in the Rocche Rosse obsidian; indeed, petrographic evidence suggests that high-strain zones may have catalyzed progressive nucleation and growth of further generations of spherulites during syn- and post-emplacement cooling.

Keywords Spherulites · Volatile elements · Lipari · Volcanic glass · CSD · Ar–Ar geochronology · NanoSIMS

Communicated by J. Hoefs.

Electronic supplementary material The online version of this article (doi:10.1007/s00410-012-0813-x) contains supplementary material, which is available to authorized users.

P. L. Clay (✉) · H. Busemann · S. C. Sherlock · S. P. Kelley
Department of Earth and Environmental Sciences, The Open University, Walton Hall, Milton Keynes MK7 6AA, UK
e-mail: Patricia.Clay@manchester.ac.uk

Present Address:
P. L. Clay
School of Earth, Atmospheric and Environmental Sciences, The University of Manchester, Manchester M13 9PL, UK

B. O'Driscoll · R. Gertisser
School of Physical and Geographical Sciences, Keele University, Keele ST5 5BG, UK

H. Busemann
School of Earth, Atmospheric and Environmental Sciences, The University of Manchester, Manchester M13 9PL, UK

Introduction

Spherulites are commonly observed features in volcanic glass (Keith and Padden 1963; Lofgren 1971a). They are characterized by the confocal radial arrangement of anhydrous (e.g., commonly quartz, cristobalite and feldspar in felsic volcanic rocks) anisotropic crystalline aggregates and are inferred to form under non-equilibrium nucleation and growth conditions (Lofgren 1971a, b). Processes of spherulite formation, in order of decreasing temperature of formation, include (1) primary crystallization upon magma degassing and quenching, with the ensuing deep undercooling of the melt ($-\Delta T \sim$ 245–350 °C; Fenn 1977; Swanson 1977; Smith et al. 2001), resulting in rapid crystallization above the glass transition temperature (T_g) (Lofgren 1971a; Baker and Freda 2001; Smith et al. 2001; Monecke et al. 2004; Castro et al. 2008), or (2) hydration and subsequent devitrification after emplacement and below T_g (Lofgren 1971a; Swanson et al. 1989). Spherulite size and distribution are controlled primarily by nucleation rate and growth rate (Keith and Padden 1963; Lofgren 1971a), and spherulites larger than 1 cm in diameter are rare (Smith et al. 2001). Nucleation sites for crystal growth are available in the form of transient, short-term crystallographic order (inherent to any silicate melt) impurities in the crystal structure or small vesicles and crystallites. Sites of short-term crystallographic order become more abundant at sub-solidus temperatures (i.e., they increase as temperature decreases) and are highly dependent upon cooling rate, until the melt has cooled to the point where ordering no longer occurs (Best 2003). Therefore, bracketing the temperature intervals over which the spherulites have crystallized is critical for interpretation of their mode of formation in a cooling lava flow. Constraining the complex crystallization dynamics involved during spherulite formation can provide information on the late-stage behavior of volatiles in melt, as well as insight into the nucleation rates, temperatures and crystallization timescales of spherulitic obsidian. More generally, the study of spherulite crystallization offers opportunities to evaluate obsidian lava flow cooling and degassing histories, as well as emplacement dynamics.

In this study, we combine textural observations with microscale quantification of glass and spherulite major and volatile element chemistry to determine the petrogenesis of spherulites in the Rocche Rosse obsidian flow (Lipari, Aeolian Islands). The historic Rocche Rosse obsidian flow is particularly valuable for this study because of its age (good preservation), its range of well-preserved and well-exposed spherulitic textures and existing constraints on emplacement history (Pichler 1980; Cortese et al. 1986; Dellino and La Volpe 1995; Gottsmann and Dingwell 2001; Daví et al. 2009; Lucchi et al. 2010). Specifically, we address whether the spherulitic texture in the Rocche Rosse obsidian is a primary textural feature resulting from high-temperature (≥800 °C) crystallization in a rhyolite magma body or whether it is a low-temperature ($\leq T_g$ 300–620 °C) product of devitrification, resulting from post-emplacement hydration and re-crystallization occurring below T_g (here, defined as a range from ~750–620 °C for rhyolite; Swanson et al. 1989; Watkins et al. 2009) in the solid state. Specifically, we define devitrification as the growth of crystalline material from solid glass, resulting from either homogenous or heterogeneous nucleation occurring below T_g. We show that chemical and volatile heterogeneities are preserved in spherulites and their obsidian host and that these heterogeneities record valuable information which can be used to reconstruct the petrogenesis of the observed spherulitic textures. Additionally, we show that the growth of spherulites in the Rocche Rosse obsidian flow started as high-temperature crystallization with subsequent solid-state textural modification.

Geological background

Geologic setting and evolution of Lipari (Aeolian Islands, Southern Italy)

Lipari is the largest of the seven islands comprising the Aeolian arc (Fig. 1), which is the result of the complex collision between the African and Eurasian plates in the Mediterranean (e.g., Caputo et al. 1972; Ninkovich and Hays 1972; Barberi et al. 1973; Scandone 1979; Gasparini et al. 1982; Beccaluva et al. 1982; Keller 1982; Anderson and Jackson 1987; De Astis et al. 2003). Lipari is one of several volcanic islands in the archipelago that are considered active (or have submarine hydrothermal vents) and last erupted in historical time (e.g., Keller 1970, 2002; Bigazzi and Bonadonna 1973; Pichler 1980; Cortese et al. 1986; Tanguy et al. 2003; Arrighi et al. 2006). It rises ~600 m above sea level (with this portion of the island being constructed over the past 223 ka; Pichler 1980; Crisci et al. 1991; Lucchi et al. 2010) emerging from a base extending ~2,000 m below sea level. Five successive eruptive epochs and related eruptions have been recognized in the geological evolution of Lipari, based on unconformity-bounded unit stratigraphy (Lucchi et al. 2010). Eruptive activity has been largely controlled by regional tectonics and characterized by shifts in vent locations across the island, eruptive style (from mainly effusive and Strombolian-type activity in the earlier eruptive epochs to effusive and predominantly hydromagmatic activity in the later eruptive epochs) and magma compositions (from calc-alkaline basalt, basaltic andesite and andesite in the earlier

eruptive epochs to high-K calc-alkaline andesite and rhyolite in the later eruptive epochs) over time. During the last eruptive epoch, from ~11 ka to historical time, volcanic activity has been concentrated in the north of Lipari with two documented successive, predominantly rhyolitic eruptions, which were characterized by initial explosive activity generating voluminous pumiceous surge (and fall) deposits (e.g., Dellino and La Volpe 1995), followed by effusion of viscous lava domes and coulées. The younger of these eruptions led to the formation of the Monte Pilato pumice cone and the obsidian-rich coulées of Forgia Vecchia and Rocche Rosse (Fig. 1; Pichler 1980; Lucchi et al. 2010).

The Rocche Rosse obsidian flow

The extrusion of the rhyolitic Rocche Rosse lava flow (denoted RRL, Fig. 1) marks the end of the latest eruptive cycle on Lipari that started with an initial, highly explosive phase that led to the deposition of voluminous pyroclastic products (MPP, Fig. 1) in NE Lipari, building a pumice cone, Monte Pilato, that opens to the NE (Lucchi et al. 2010). The Rocche Rosse lava poured out of the Monte Pilato crater, flowing some 2 km to the NE to reach (and extend) the existing coastline (Fig. 1). It is an obsidian-rich lava flow (or coulée), up to 60 m thick, with well-developed flow foliation, a blocky surface characterized by

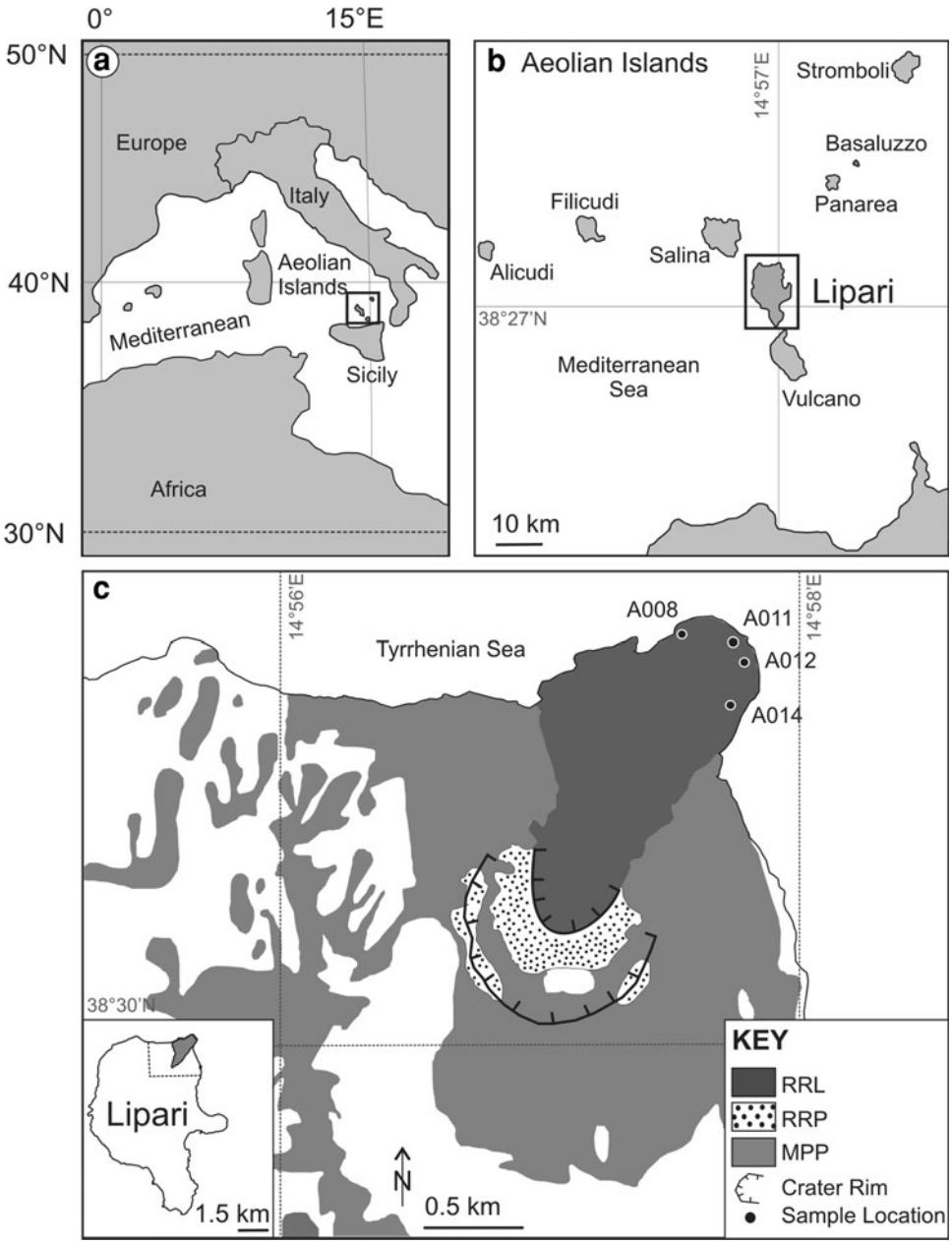

Fig. 1 **a** Location map of the Aeolian Islands. **b** Location of Lipari relative to other Aeolian Islands. **c** Simplified geologic map of the northeastern tip of Lipari. Generalized volcano-stratigraphic units of the Monte Pilato—Rocche Rosse sequence. *RRL* Rocche Rosse obsidian flow, *RRP* Rocche Rosse pyroclastics, *MPP* Monte Pilato Products. Modified and adapted from Cortese et al. (1986) and Dellino and La Volpe (1995). Grid references are given in Table 1

curved fractures and ogive structures as well as characteristic ramp structures (Cas and Wright 1987; Lucchi et al. 2010). Over the past few decades, several attempts have been made to date both the pumice sequence and subsequent obsidian lava of the youngest eruption cycle on Lipari, using fission track and radiocarbon dating techniques as well as interpretations based on historical documents (Keller 1970, 2002; Bigazzi and Bonadonna 1973; Pichler 1980; Cortese et al. 1986; Tanguy et al. 2003; Arrighi et al. 2006). The picture that has emerged is that the Rocche Rosse flow (and, most probably, also the Forgia Vecchia) represents an episode of renewed activity several hundred years after the initial explosive events that built the Pilato pumice cone. In the latest attempt to constrain the age of the initial eruption phase of Monte Pilato, Keller (2002) reports a calendar date of 776 AD obtained on short-lived plant remains directly from the base of the Pilato pumice deposits, emphasizing the coincidence of this age with a report of Gregorius, which, in contrast to earlier documents, refers specifically to volcanic activity on Lipari and suggests that in 787 AD the island was still in eruption (Keller, personal communication 2012). For the Rocche Rosse obsidian flow, an archeomagnetic date of 1,220 (±30) AD (Tanguy et al. 2003), an age later revised to 1,230 (±40) AD (Arrighi et al. 2006), testifies to the latest eruptive activity on Lipari.

The preservation of fresh glass and the proportion of glass to crystalline material in the Rocche Rosse flow both are highly variable (refer to photographs in Figs. 2, 3). Areas almost entirely dominated by crystalline material are locally observed (Fig. 2a). In some instances, the occurrence of crystalline material can be linked to structures within the outcrops. For example, the hinge zones of (<1 to >10 m amplitude) folds and the spaces between boudins often contain much more crystalline material than glass, relative to adjacent parts of the outcrop that form a different part of the structure in question, i.e., the fold limbs. Foliation in the obsidian is principally carried by trails of spherulites (Fig. 2a–e), which separate bands of glass that contain populations of spherulites isolated from one another. The spherulites in the trails may be either completely separated from one another (though contained within the same plane) or touching one another. Thin (≤1 mm) bands of completely conjoined spherulites also carry the foliation (Fig. 2d, e, i). No simple pattern is discernible in the orientation of the foliation across the flow (Fig. 2a), and a wide variety of additional complex structures are evident at the centimeter to tens of meter scales. For example, millimeter-thick low-angle (to the foliation) microshears, filled with crystalline material, are common as are sheath folds (defined by spherulitic bands and with wavelengths of centimeters to tens of meters), stretching lineations and tension gashes (Fig. 3). Some of these deformation features in the Rocche Rosse obsidian flow have been previously noted (Cabrerra et al. 2011). The intensity of deformation observed in the Rocche Rosse obsidian is therefore comparable to other obsidian flows, such as Little Glass Mountain, California (Fink 1983), the Big Obsidian flow, Oregon (Rust and Cashman 2007), and obsidian flows of the Inyo domes, California (Castro et al. 2002).

Sample petrography

Samples were collected over a kilometer-long traverse of the Rocche Rosse flow with the aim of capturing a wide variety of glass and spherulitic textures and intergrowths (sample locations are given in Fig. 1). Estimates of relative glass and spherulite proportions were obtained from digitized thin-section images; typically, 2–30 vol% of the total crystalline material is in spherulitic form in a glass matrix of rhyolitic composition (5–70 vol%). The observed textures demonstrate a bimodal distribution: spherulites are either isolated individually in the glass or form dense trails and bands. Spherulite texture in the Rocche Rosse obsidian has previously been described in several studies (e.g., Cole and Butler 1892; Dellino and La Volpe 1995; Gimeno 2003), and it is not intended to duplicate that work here. However, for the most part the observations below have not previously been documented. The dominant spherulite texture consists of individual spherulites, isolated in the glass matrix and not impinging on other spherulites (Fig. 2e). These spherulites typically range from 0.1 to 2.0 mm in size. Crystalline material is radially arranged as shown in Fig. 2e, f, j. X-ray diffraction experiments carried out on spherulite powders show that the spherulites consist of a SiO_2 polymorph (predominantly cristobalite) and K-feldspar (orthoclase) (Fig. 4). Void space is common in the central portion of the spherulite (Fig. 2f, h). Spherical microfractures are observed around the margins of some isolated spherulites (Fig. 2h; refer also to BSE images in Fig. 5). Thin rims of crystalline material, distinct from glass and spherulite, are often observed to occupy the space between spherulite and glass (Fig. 2f, h). In other samples, the interface between glass and spherulite is occupied by a rim of reddish-colored glass of variable thickness (0.1–0.5 mm) (Fig. 2g, i). This difference in color between the rim (reddish-brown) and the glass (clear) probably reflects a change in oxidation state of Fe in the glass, as documented by Castro et al. (2008, 2009).

Trails of single spherulites are observed to be laterally continuous over tens of meters and often form 0.1- to 1-mm-wide bands (Fig. 2a, d, e). These spherulite bands provide the principal visible anisotropy to the obsidian and are what allow some of the more complex folding described above to be deduced. In some examples, spherulites

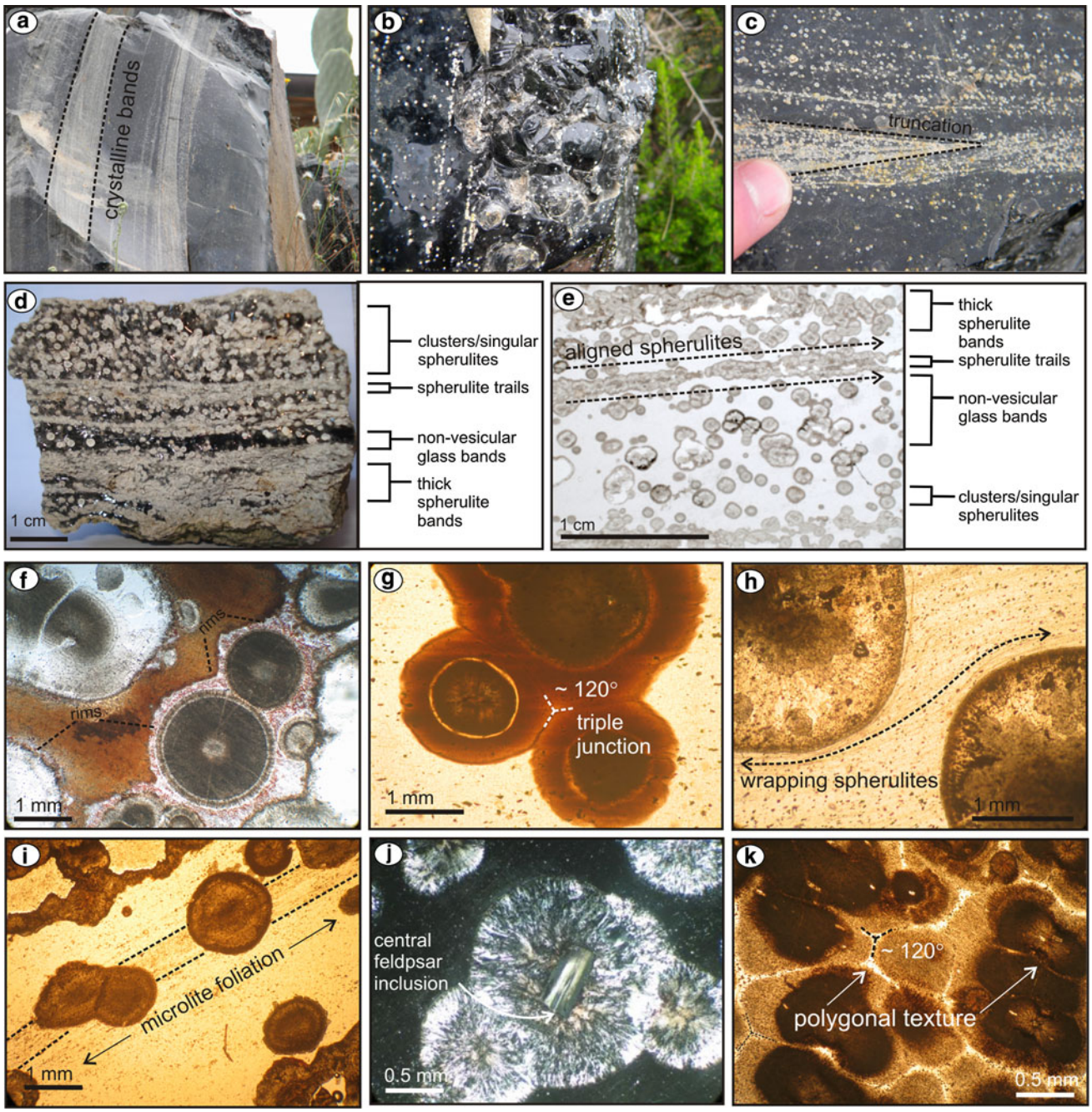

Fig. 2 **a** Field exposure of the Rocche Rosse obsidian flow, showing the aligned bands of spherulites. *Dotted lines* demarcate large continuous flow band in the crystalline material. Width of fresh glass outcrop is ~1.5 m. **b** Perlitic cracks in the Rocche Rosse flow. Cracks are roughly 0.5–1.0 cm in diameter. Note pencil tip for scale. **c** Truncated spherulite trails in the Rocche Rosse obsidian (noted by *dashed lines*). **d** Hand specimen (sample LIP-01) showing the texture and distribution of the different spherulite groups: Single spherulites, clusters, linear trails and *thick* spherulite bands as well as zones of non-vesicular glass with minor spherulites (all labeled). **e** Photomicrograph of sample LIP-02 highlighting the same textural features (as in **d**). **f** Photomicrograph showing impinging spherulites with radiating confocal crystallites, spherulite rim and growth front. **g** Photomicrograph showing cluster morphology and 120° angles (highlighted by *dashed lines*) between growing spherulites. **h** Photomicrograph showing fabric with aligned microlites wrapping (noted by *dashed line*) around two isolated spherulites. **i** Photomicrograph showing individual spherulites in a flow fabric with aligned microlites (between *dashed lines*). Note the absence of the fabric in the glassy areas devoid of spherulites. **j** Photomicrograph of spherulite cluster. Central spherulite has nucleated around a small orthoclase microlite at its center. **k** Photomicrograph of densely packed mature spherulites achieving polygonal boundaries from solid-state modification of the spherulitic texture

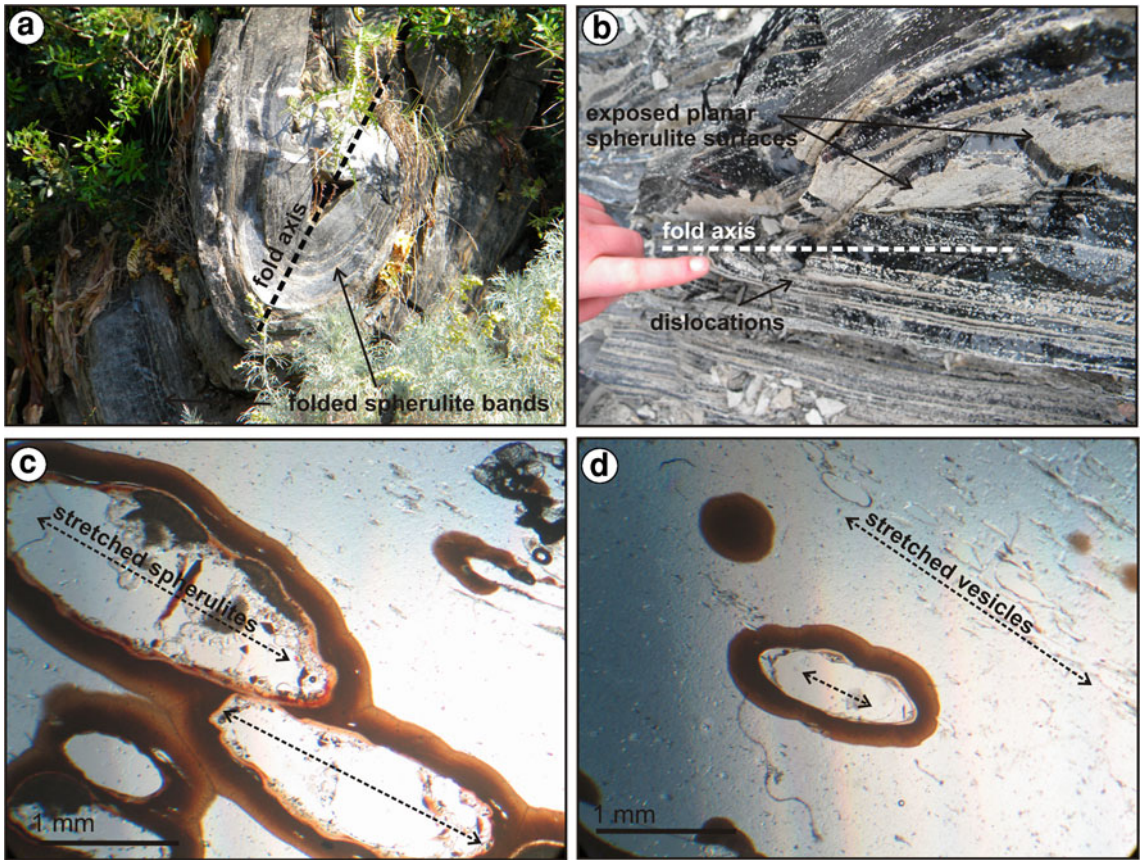

Fig. 3 Deformation features in the Rocche Rosse obsidian. Folds shown in **a** (the *dashed line* shows the fold axis, and *arrows* point to folded bands of spherulites) and **b** are typical of the Rocche Rosse obsidian flow and often complex. Evidence for deformation to the spherulitic textures is observed in some sections, as in the photomicrographs shown in **c** and **d**, where stretching occurs in both the spherulites and glass (highlighted in **c** and **d** by *arrows*)

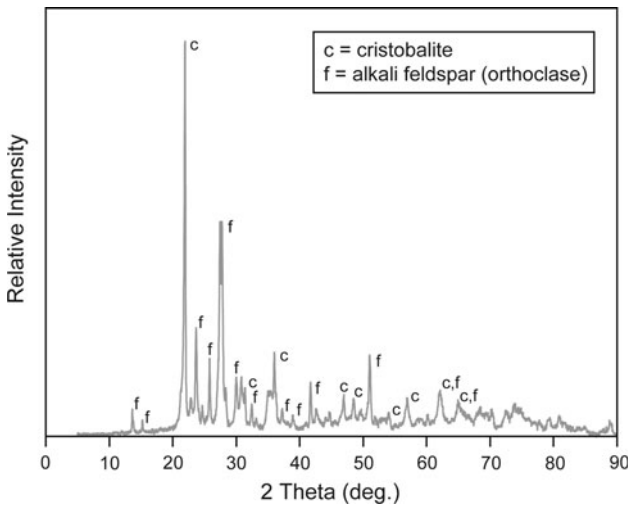

Fig. 4 X-ray diffraction pattern for a Rocche Rosse spherulite-bearing obsidian sample, with the main peaks for cristobalite (*c*) and alkali feldspar (orthoclase) (*f*) labeled. The powdered rock sample was placed in a flat disk sample holder and scanned on a Bruker D8 Advance X-ray diffractometer at Keele University using CuKα radiation, a scan range from 5° to 90° (2 Theta), a 0.03° (2 Theta) step size and a data collection time of 30 s per step

occupy nearly 100 % of the observed bands, such that identifying individual spherulites is difficult. In such cases, thick bands of spherulites, 2–3 mm thick, form laterally continuous, parallel bands of spherulites with complex internal structure (Fig. 2d). There is also evidence in the outcrops that such bands have accommodated significant amounts of dislocation (from several centimeters up to several meters; Fig. 3b). Where glass is observed to be fresh, the groundmass contains numerous small microlites (<0.01 mm; Fig. 2g, h, i) and, more rarely, phenocrysts of K-feldspar (Fig. 2j). In several samples, such crystals occur at the centers of larger spherulites ($\sim$2 mm in diameter; see Fig. 2j). The microlites lie within the strong penetrative foliation defined by the spherulite bands, confined to layers <1 mm thick in the obsidian. Notably, this foliation commonly occurs in the glass between individual trail-forming spherulites, but is absent on either side of the trails. The foliation in the glass may subtly wrap spherulites, that is, deflect around them (e.g., as in Fig. 2h), but more commonly there is complete discordance between the alignment of microlites and the outer margins of spherulites (Fig. 2i). Where reddish-colored rims or associated

microfractures occur at spherulite margins, as described above, the foliation is clearly overgrown by these structures (Fig. 2g). Indeed, the rims sometimes exhibit ragged edges developed parallel to the foliation, suggesting mimetic growth along the foliation planes. Spherulites rarely show signs of flattening into elliptical geometries, parallel or sub-parallel to the foliation in the obsidian (Fig. 3c, d). Impinging spherulites and clusters or botryoidal forms (e.g., Fig. 2g) also rarely occur. Impinging spherulites conjoin along one edge and range in size from 1 to 2.6 mm (Fig. 2). Botryoidal spherulites contain three or more conjoined spherulites, often with a dominant large cluster of two spherulites flanked by adjoining smaller spherulites with less well-defined internal structures. Clustered spherulites often exhibit a well-developed polygonal texture, in which the reddish rims (or other overgrowth rims on spherulites) display triple junctions that meet at well-defined dihedral angles of $\sim 120^{\circ}$ (e.g., Fig. 2g). This texture is particularly noticeable in samples that have unusually high concentrations of spherulites ($\geq$75 vol%).

Sample preparation and methods

Quantitative textural analysis

Crystal size distribution (CSD) analysis provides a quantitative measure of the number of crystals of a given mineral phase, or as for this study, spherulites, per unit volume within a series of defined size intervals (see Higgins 2006a for a review). It has been argued that simple crystallization (in either of the end-member batch or open-system models exclusively; Marsh 1998) leads to a straight, or log-linear, CSD plot representing kinetic textures solely developed through nucleation and growth (Higgins 2006b). Kinking or curvature in the CSD plot profile has been attributed to different processes that modify or add to the original crystal population (Higgins 2006a), examples being crystal accumulation and removal (Marsh 1998), compaction (Boorman et al. 2004), mixing of crystal populations (Higgins 1994; Jerram et al. 2003; Turner et al. 2003) and post-nucleation crystal coarsening caused by annealing or Ostwald ripening (Boorman et al. 2004). For the present study, CSDs were determined from 14 thin sections using the methods of Higgins (2000) and the program *CSDCorrections 1.37* to complement the mineral chemical and volatile data in investigating the processes of spherulite nucleation and crystallization. The principal objective of this analysis is to assess, from visual comparison of CSD plots and other CSD parameters (see below), how closely the nucleation and growth histories of spherulite populations from different parts of the flow compare with one another.

A variety of spherulite textures were arbitrarily chosen for CSD quantification; samples in which the population densities of spherulites that are isolated in their glass groundmass vary considerably in hand specimen and under the microscope (in terms of spherulite diameter and concentration, as described above) were specifically targeted. Spherulites in bands were avoided, as the margins of these are not always distinguishable from adjacent spherulites. The CSDs were calculated from measurements carried out on digitized photomicrographs using the image analysis software *ImageJ*. CSD data are usually plotted as population density (logarithmic number of crystals per unit volume) against crystal size (maximum length). In this study, the radius of a circle with an area equal to that of the measured spherulite is adopted as the measured crystal size parameter. This approach means that an aspect ratio of 1:1:1 and roundness value of "one" are input into the *CSDCorrections* software, bypassing many of the thin-section "cut effect" issues that can arise from the stereological 2D-to-3D conversion of anisotropic crystals (Boorman et al. 2004; Higgins 2006a, b). The smallest spherulites measured (at 25 times magnification) were $\sim$0.1 mm in size. As they are typically easily visible against their glass groundmass, it is assumed that all spherulites have been measured for each sample and therefore that CSD behavior at small size fractions is not an artifact of the measurement process. CSD results are shown in Fig. 5 (refer to section "CSD results").

Electron microprobe (EMP) analysis

Major element chemistry of glass and spherulites (samples A and B) was determined by EMP using a Cameca SX 100 at The Open University. Typical peak count times between 10 and 40 s were used to minimize the potential for volatilization of the glass during analysis. A 10–15 μm spot size, an acceleration voltage of 20 kV and a beam current of 20 nA were used. Mineral and glass standards were analyzed periodically, typically at the start of and midway through each day. For complete details including peak and background count times, calibration species and detection limits, refer to Supplementary Electronic Material 1. Average glass data are given in Table 2, and the full data set, including all spherulite transects shown in Fig. 6, is provided in Supplementary Electronic Material 1.

Secondary ionization mass spectrometry (NanoSIMS)

Volatile measurements (CO_2 as ^{12}C, H_2O as $^{16}O^1H$, ^{19}F, ^{35}Cl and ^{32}S, all measured as negative ions (relative to ^{30}Si)) in five polished glass chips and one polished spherulite (sample A) were carried out on the Cameca

NanoSIMS 50L at The Open University (Table 3). Five 1–3-mm-sized pieces of Rocche Rosse obsidian and one complete polished spherulite were embedded in indium metal (Alfa Aesar "puratronic" 5 mm shot, Product # 10,615, 99.999 % purity) along with standard glasses (see Clay 2010 for details) within aluminum mounts (1-inch diameter, suitable for NanoSIMS standard "geology" holder). Samples were polished using silica carbide and diamond paste down to 1 μm grain size, then further polished with Al_2O_3 (1 μm) and cleaned ultrasonically in methanol and boron-free water before being dried in a vacuum oven. The mount was coated with a 20–30-nm-thick conductive gold layer prior to analysis (Hauri et al. 2002; Saal et al. 2008).

Two standard glasses and other geo-reference materials were used to construct a calibration for the analysis of C^-, OH^-, F^-, Cl^- and S^-. CO_2 is measured as C^-, and H_2O as OH^- (Hauri et al. 2002). NIST standard reference materials (SRM) 610 and 612 were used in addition to geo-reference materials which consisted of basaltic glasses ALV-519-4-1, GL-D30-1 and GL-D52-5 (all volatile concentrations and corresponding references given in Electronic Supplementary Material 2). San Carlos olivine and a synthetic forsterite ($SynFo_{68}$) were used as nominally anhydrous minerals to give a constraint on the detection limit blank during analysis.

The primary Cs^+ beam (at 16 keV) current used for analysis and pre-sputtering was 1–1.2 nA, along with a 300–335 nA electron current, to counteract any charge buildup on the glass sample surface. Negative secondary ions were collected simultaneously in multi-collection mode on six of the seven electron multipliers ($^{35}Cl^-$ on fixed detector 7). The Cs^+ primary beam was rastered in 64 × 64 pixels over a 12-μm square on the sample surface, with the inner 4.5 × 4.5 μm (24 × 24 pixels) square reserved for analysis for well-defined sampling without contributions from the crater rims. Pre-sputtering was performed for ~3 min through the gold coating for sample cleaning, removing surface contamination layers for improved charge compensation. Pressure in the sample chamber often reached 1.3×10^{-8} Pa and was typically $\leq 8 \times 10^{-8}$ Pa during analyses. During the analysis each species was measured 50 times, for 1 s per step, leading, including automated peak and further lens voltage centering (peak centering on $^{35}Cl^-$, "EOS," and "SIB horizontal/vertical") to ~10 min total data collecting time per analysis.

We estimate the maximum random error of measurement to be no greater than 10 % for H_2O and CO_2, Cl and S and no greater than 15 % for F based on the variation of the results obtained for the various analyses in each sample. This estimate encompasses (1) uncertainties of each measurement, (2) sample heterogeneity and most importantly (3) the uncertainty of the calibration lines. Typical uncertainties due to counting statistics (Poisson) are ≤1 % for all ratios except for $^{12}C/^{30}Si$ (≤3 %) and hence small compared to the other contributions to the error.

Calibration lines were constructed for each volatile species plotting volatile concentrations in standards versus the measured ratio of the volatile $x/^{30}Si^-$ (where x = $^{12}C^-$; $^{17}OH^-$; $^{19}F^-$; $^{32}S^-$ and $^{35}Cl^-$; refer to Clay 2010 for details). The sample ratios were normalized to a SiO_2 content of 50 % to account for potential spread in SiO_2 content between the standard glass and sample. This was done following the method of Hauri et al. (2002). Calibrations are linear for F, Cl and S, and the water calibration is treated as linear for the concentrations represented in the present study (H_2O calibration is linear in rhyolite up to ~7 wt% H_2O; Tenner et al. 2009), and free of matrix effects. In general, standard data fit very well linearly (Electronic Supplementary Material 3), with R^2 values of 0.92–1.00, with the exception of F due to variations in recommended values in the geo-reference materials (R^2 = 0.79–0.80). Detection limits were calculated to be: H_2O ~ 60 ppm; CO_2 ~ 12 ppm; F ~ 5 ppm; Cl ~ 5 ppm and S ~ 5 ppm, based on concentrations measured in a nominally anhydrous mineral (San Carlos olivine).

Ar–Ar sample preparation and methods

Rocche Rosse obsidian samples were included for Ar–Ar analysis to provide qualitative constraints on the distribution and behavior of Ar in the glass and spherulites, as part of a larger study on testing the application and limits of the Ar–Ar geochronometer to glass (Clay 2010; Clay et al. 2011). Sample (A) were crushed and whole spherulites were removed from the glass matrix. Shards of glass, approximately 1–2 mm in size, were selected for analysis (approximately 100 mg). Whole spherulites, approximately 1–2 mm in diameter, were picked and cleared of minimal adhered glass. All samples were cleaned ultrasonically in acetone for 30 min followed by deionized water for an additional 20 min and further dried at low temperature (~60 °C). Samples and standards were irradiated at the McMaster Reactor, Canada, for 1 h. Biotite standard GA-1550 (age = 98.8 ± 0.5 Ma; Renne et al. 1998; McDougall and Harrison 1999) and sanidine standard TCR-2 (Taylor Creek Rhyolite, age = 27.92 ± 0.04 Ma, Duffield and Dalrymple 1990) were used as neutron fluence monitors (Electronic Supplementary Material 4).

Glass and spherulites were step-heated with a New Wave NdYAG 1,064 nm IR laser. All measurements were made on a MAP-215-50 noble gas mass spectrometer. Two SAES getters (one running at 400 °C and one at room temperature) cleaned the extracted gas prior to analysis. Samples were slowly step-heated and eventually fused over

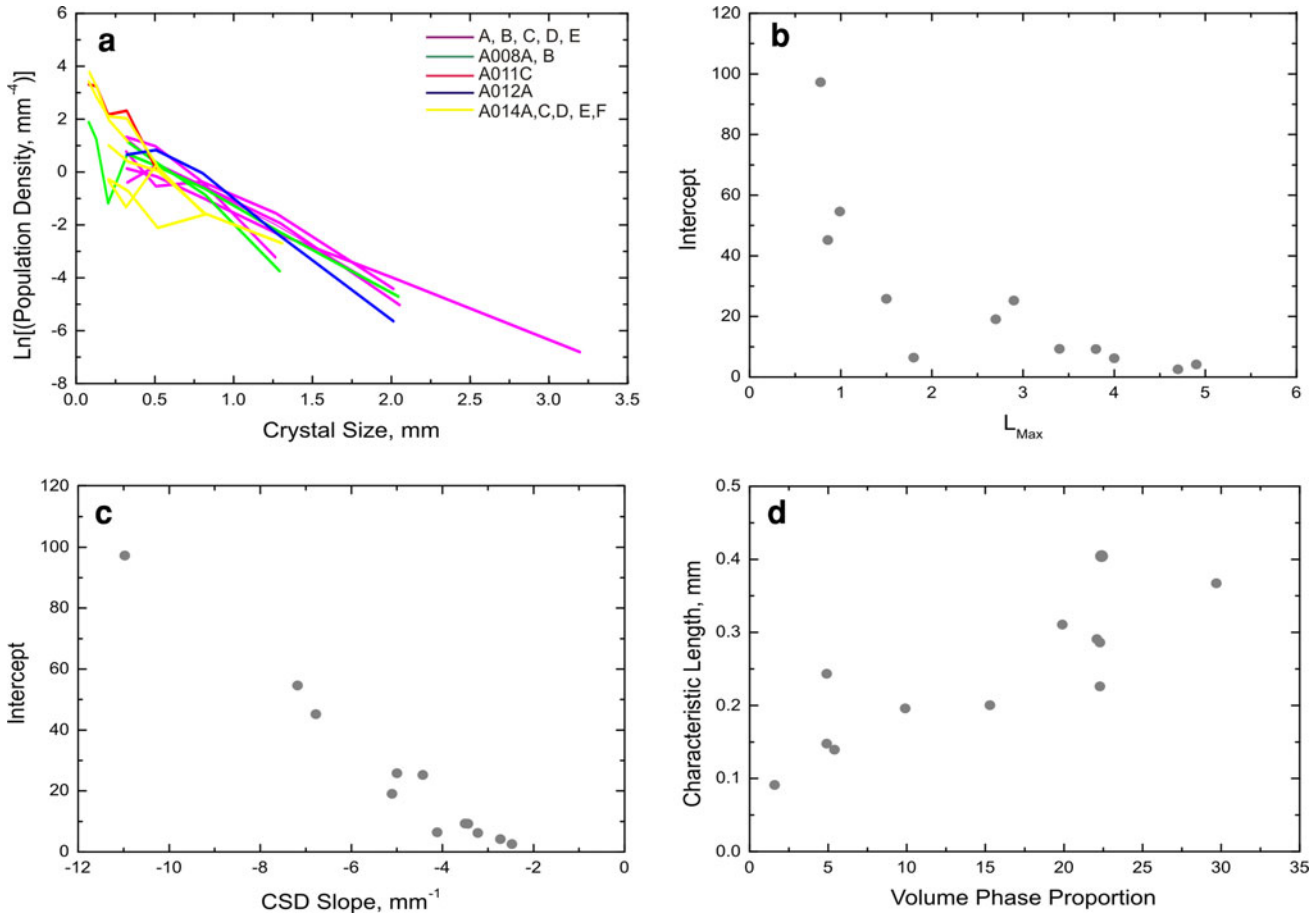

Fig. 5 Results of CSD analysis. **a** Ln (population density) versus crystal size by sample. **b** Intercept versus L_{max}. **c** Intercept versus CSD slope. **d** Characteristic length versus volume phase proportion. Refer to section "CSD results"

the course of ten (glass) and eight (spherulite) steps. Fifteen measurements were made per cycle for each isotope with a total of ten cycles. Gas was forced through a liquid N_2-cooled "u-bend" cold trap prior to analysis. Reported Ar–Ar errors are random errors at the 2σ confidence level which incorporate a 0.5 % error assigned to the J value. Data were corrected for instrument blanks, mass discrimination, atmospheric argon ($^{40}Ar/^{36}Ar = 298.56 \pm 0.31$; Lee et al. 2006) decay of ^{37}Ar ($t_{1/2} \sim 35.1$ days) and ^{39}Ar ($t_{1/2} \sim 269$ years) and reactor-induced interferences on ^{40}Ar, ^{39}Ar and ^{36}Ar using "ArMaDiLo" (Argon Macro Direct Loader) and plotted using Isoplot 3.0 (Ludwig 2003).

Results

CSD results

The CSD plots are illustrated in Fig. 5, keyed to specific localities in the Rocche Rosse flow (Fig. 1). The important input and output textural parameters from the *CSDCorrections* program for all samples measured are presented in Table 1. Many of the CSDs show considerable complexity and heterogeneity at smaller size fractions (i.e., below ~0.5 mm crystal diameter; Fig. 5a). However, much greater similarity is observed at larger size fractions, where all of the plots have log-linear profiles. Slope values, calculated for 12 of the 14 CSDs by subjecting the data to least squares regression using Microsoft Excel, range between −2.5 and −10.9 mm^{-1}. Most (i.e., 9 of 12) of these CSDs fall into the steeper (−2.5 to 5.1 mm^{-1}) side of this range, suggesting the presence of a dominant population of spherulites (i.e., with relatively similar slopes). Plots of the Y-intercept, a proxy for nucleation density, against CSD slope and L_{max} (taken here as the average radius of the four largest spherulites in each sample) show well-developed negative correlations (Fig. 5b). Higgins (2002) showed that the relationship between characteristic length and the volume phase proportion can be useful in discriminating separate mineral phase populations or establishing relationships within the CSD data set. For the Rocche Rosse spherulite data, these parameters exhibit a strong positive correlation (Fig. 5d). This supports the

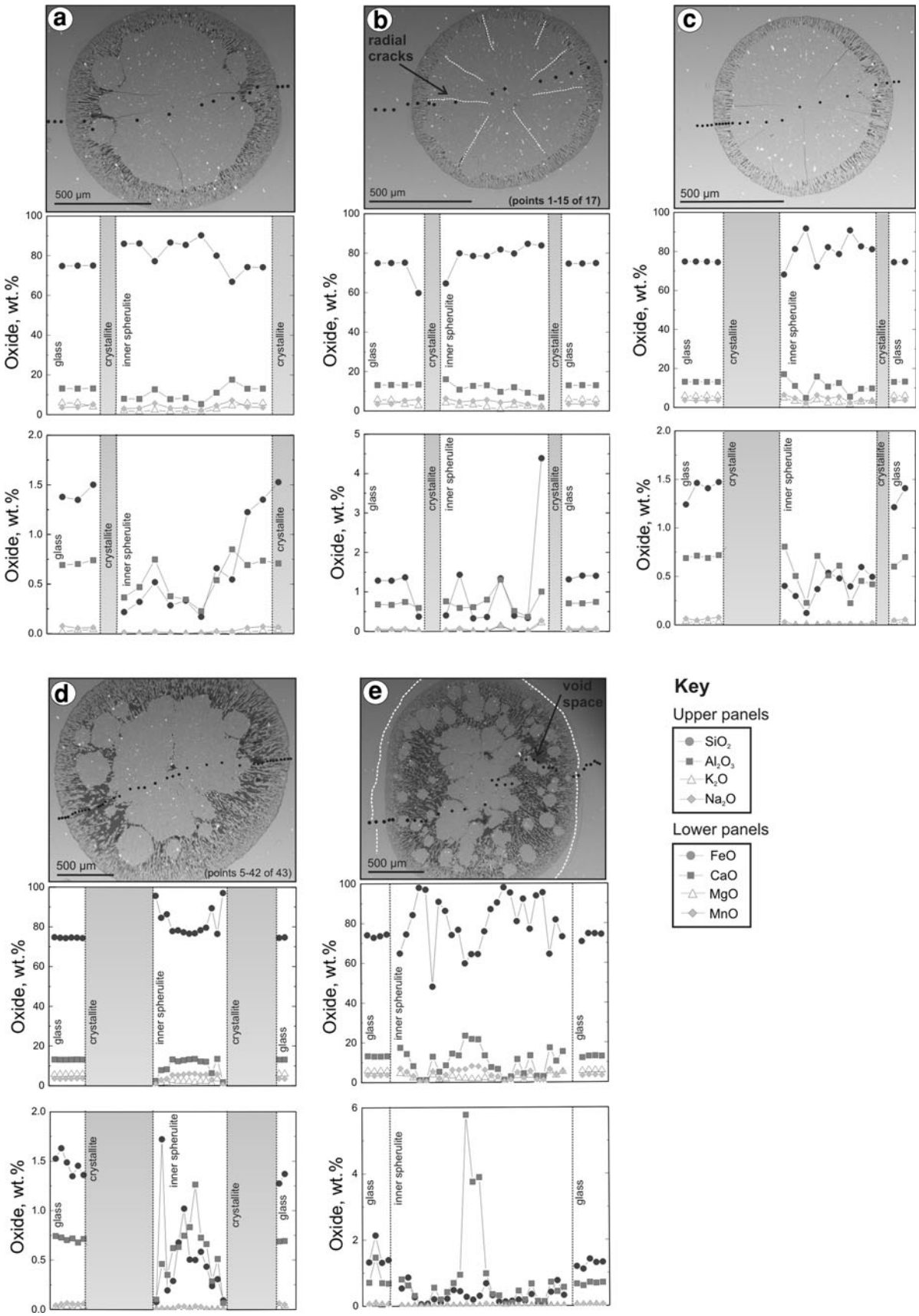

◀ **Fig. 6** Backscattered electron (BSE) images of sample LIP02 and corresponding major- and minor-oxide chemistry from electron microprobe transects (refer to section "EMP results: glass and spherulite chemistry"). The major elements (as oxides) (SiO_2, Al_2O_3, K_2O and Na_2O) and distributions across each spherulite transect are given in the *upper panels,* and minor elements (FeO, CaO, MgO and MnO) and distributions are given in the *lower panels*. **a** Single spherulite-1; **b** single spherulite-2; **c** single spherulite-3; **d** single spherulite-4 and **e** spherulite cluster B. Full data set for each transect can be found in the Electronic Supplementary Material 1. Note: not all points (particularly data points in bulk glass) are visible in the BSE image; therefore, not all points align visually with the corresponding transect. White *dashed lines* in **b** indicate small radial fractures and in **e** highlight small spherical fractures sometimes observed around the spherulites. Points removed from the crystallite/spherulite boundary reflect instances of low totals, likely from mixed analyses

suggestion above that despite being calculated from sample thin sections with apparently different spherulite textures, the CSDs reflect similar and comparable nucleation and growth behavior across all 12 samples.

EMP results: glass and spherulite chemistry

In order to obtain average glass compositional data, thirty EMP analyses of glass in two samples (samples A and B) were measured in areas spatially removed from spherulitic textures. Due to consistency between analyses, these points were averaged and taken as representative of the overall bulk glass chemistry (refer to Table 2; but see full EMP data set available in the Electronic Supplementary Material 1). The glass is a high-Si rhyolite, with an average SiO_2 content of 74.9 ± 0.2 wt% and average total alkalis ($Na_2O + K_2O$) of 9.5 ± 0.1 wt%. Transects from glass across each spherulite type were carried out to document any chemical heterogeneities with textural variations in the glass (Fig. 6). Figure 6 shows the results of 5 of 6 transects made (the longest transect performed along a spherulite band is not shown due to the large number of points taken over a large area; refer to Electronic Supplementary Material 1 for data) in conjunction with a backscattered electron (BSE) image of the spherulite across which the transect was taken. Determination of crystalline compositions in the inner crystallite boundary was attempted but often yielded low totals or non-stoichiometric compositions (Electronic Supplementary Material 1). This is due to the extremely fine-grained nature of the crystal intergrowths leading to mixed analyses. Where successful, feldspar compositions of $Ab_{70}Or_{30}$ were determined.

Table 1 Results of crystal size distribution (CSD) analysis

Sample no[a]	Measured area (mm^2)	No of crystals	R^2	CSD slope (mm^{-1})	Intercept	C_L	Volume phase prop. (%)	L_{max}
A (LIP-01)	983.4	246	0.99	−2.47	2.54	0.40	22.4	4.7
B (LIP-02)	575.9	263	0.98	−5.00	25.77	0.20	15.3	1.5
C	556.4	221	0.99	−3.44	9.21	0.29	22.1	3.8
D	623.8	195	0.99	−3.50	9.31	0.29	22.3	3.4
E	630.1	213	0.98	−2.72	4.17	0.37	29.7	4.9
A008A	988.3	322	0.99	−5.11	19.03	0.20	9.9	2.7
A008B	1,196.2	407	0.99	−3.22	6.19	0.31	19.9	4
A011C	416.4	270	0.9	−7.18	54.59	0.14	5.4	0.99
A012A	1,157	550	0.99	−4.43	25.22	0.23	22.3	2.9
A014A								
A014C	361.5	130	0.97	−10.97	97.20	0.09	1.6	0.78
A014D								
A014E	827.4	168	0.98	−4.11	6.41	0.24	4.9	1.8
A014F	790.9	431	0.95	−6.78	45.20	0.15	4.9	0.86

[a] Grid references (UTM Zone 33 S): A08A and A08B: 496105 4263646; A011C: 496233 4263679; A012A: 496267 4263715; A014A–A014F: 49631 4263500; A–E: 496400 4263480

Table 2 Average electron microprobe data of Rocche Rosse glass ($n = 30$)

	SiO_2	TiO_2	Al_2O_3	FeO	MnO	MgO	CaO	K_2O	Na_2O	F	Cl	Total[a]
Glass	74.9	0.07	13.2	1.40	0.06	0.03	0.71	5.7	3.8	0.14	0.33	100.2
SD	0.2	0.02	0.04	0.15	0.01	0.01	0.02	0.06	0.09	0.06	0.02	0.1

Measurements were made on a Cameca SX100 at the Open University. All values are in wt %. The full data set is available in Electronic Supplementary Material 1

[a] In the case of F and Cl, the oxygen equivalents are calculated by (moles F × 0.4211) and (moles of Cl × 0.2256) which are subsequently subtracted from the total

Table 3 H_2O, CO_2, F, Cl and S concentrations in glass and across the spherulite transect shown in Fig. 7

	H_2O	±	^{12}C	±	^{35}Cl	±	^{19}F	±	^{32}S	±
Bulk glass										
LIP-01-1	0.103	0.004	b.d[a]	–	4,190	590	950	210	b.d	–
LIP-01-2	0.105	0.004	b.d	–	3,840	550	920	210	b.d	–
LIP-01-3	0.114	0.004	b.d	–	4,830	690	1,020	230	b.d	–
LIP-01-4	0.100	0.004	b.d	–	4,120	590	940	210	b.d	–
LIP-01-5	0.083	0.003	b.d	–	4,260	600	960	210	b.d	–
LIP-01-6	0.081	0.003	b.d	–	3,790	540	920	210	b.d	–
LIP-01-7	0.080	0.003	b.d	–	3,800	540	880	200	b.d	–
LIP-01-8	0.084	0.003	b.d	–	4,120	580	960	220	b.d	–
LIP-01-9	0.084	0.003	b.d	–	4,130	590	970	220	b.d	–
LIP-01-10	0.084	0.003	b.d	–	4,430	630	970	220	b.d	–
LIP-01-11	0.076	0.003	b.d	–	3,580	510	910	200	b.d	–
LIP-01-12	0.081	0.003	b.d	–	3,940	560	940	210	b.d	–
Average/SD	0.089	0.012	b.d	–	4,090	330	950	40	b.d	–
Transect[b]										
LIP-01-T1	0.098	0.004	80	10	4,450	630	1,020	230	b.d	–
LIP-01-T2	0.095	0.003	20	5	3,810	540	970	220	b.d	–
LIP-01-T3	0.094	0.003	b.d	–	3,400	480	930	210	b.d	–
LIP-01-T4	0.075	0.003	630	30	2,084	300	700	160	b.d	–
LIP-01-T5	0.104	0.004	b.d	–	3,330	470	930	210	b.d	–
LIP-01-T6	0.107	0.004	b.d	–	3,750	530	950	210	b.d	–
LIP-01-T7	0.112	0.004	b.d	–	4,060	580	960	220	b.d	–
LIP-01-T8	0.116	0.004	b.d	–	3,790	540	1,060	240	b.d	–
RIM	n.d	–	n.d	–	n.d	–	n.d	–	n.d	–
RIM	n.d	–	n.d	–	n.d	–	n.d	–	n.d	–
RIM	n.d	–	n.d	–	n.d	–	n.d	–	n.d	–
LIPT-01-T9	0.008	0.000	170	40	3,200	480	240	60	b.d	–
LIPT-01-T10	0.011	0.001	290	50	2,360	340	210	50	b.d	–
LIPT-01-T11	0.089	0.011	b.d	–	2,870	420	210	50	130	10
LIPT-01-T12	0.027	0.001	3,400	250	1,200	180	170	40	70	5
LIPT-01-T13	0.085	0.005	11,340	1,300	11,985	180	150	30	110	10
LIPT-01-T14	0.040	0.002	5,700	510	660	100	130	30	120	10
LIPT-01-T15	0.054	0.003	13,400	880	2,590	380	180	40	90	5
LIPT-01-T16	0.006	0.000	50	10	6,770	970	310	70	b.d	–
LIPT-01-T17	0.006	0.000	b.d	–	7,740	1,140	200	50	b.d	–
LIPT-01-T18	0.006	0.000	8	4	7,260	1,050	200	50	b.d	–
LIPT-01-T19	0.007	0.000	b.d	–	1,900	270	270	60	b.d	–
LIPT-01-T20	0.011	0.001	860	90	4,980	750	180	40	b.d	–
LIPT-01-T21	0.023	0.003	2,740	580	4,400	640	220	50	30	5
LIPT-01-T22	0.033	0.002	6,000	580	500	70	80	20	110	10
LIPT-01-T23	0.163	0.007	16,200	1,100	670	100	140	30	80	5
LIPT-01-T24	0.023	0.001	5,300	480	640	100	120	30	120	10
LIPT-01-T25	0.093	0.004	5,400	320	530	80	160	40	50	3
LIPT-01-T26	0.047	0.003	11,100	1,600	2,550	370	200	50	140	10
LIPT-01-T27	0.029	0.004	9,930	2,920	2,930	430	220	50	2.7	0.3
RIM	n.d	–	n.d	–	n.d	–	n.d	–	n.d	–
RIM	n.d	–	n.d	–	n.d	–	n.d	–	n.d	–
LIPT-01-T28	0.116	0.004	b.d	–	3,910	560	1,820	410	b.d	–
LIPT-01-T29	0.114	0.004	b.d	–	3,240	460	1,030	230	b.d	–

Volatile concentrations were measured on a Cameca 50L NanoSIMS at The Open University. Concentrations are in ppm with the exception of H_2O which is given in wt%. Errors are 2σ

[a] *b.d.* below detection, *n.d.* not determined due to analytical challenges associated with heterogeneous microcrystalline material

[b] Transect corresponds to points in Fig. 7

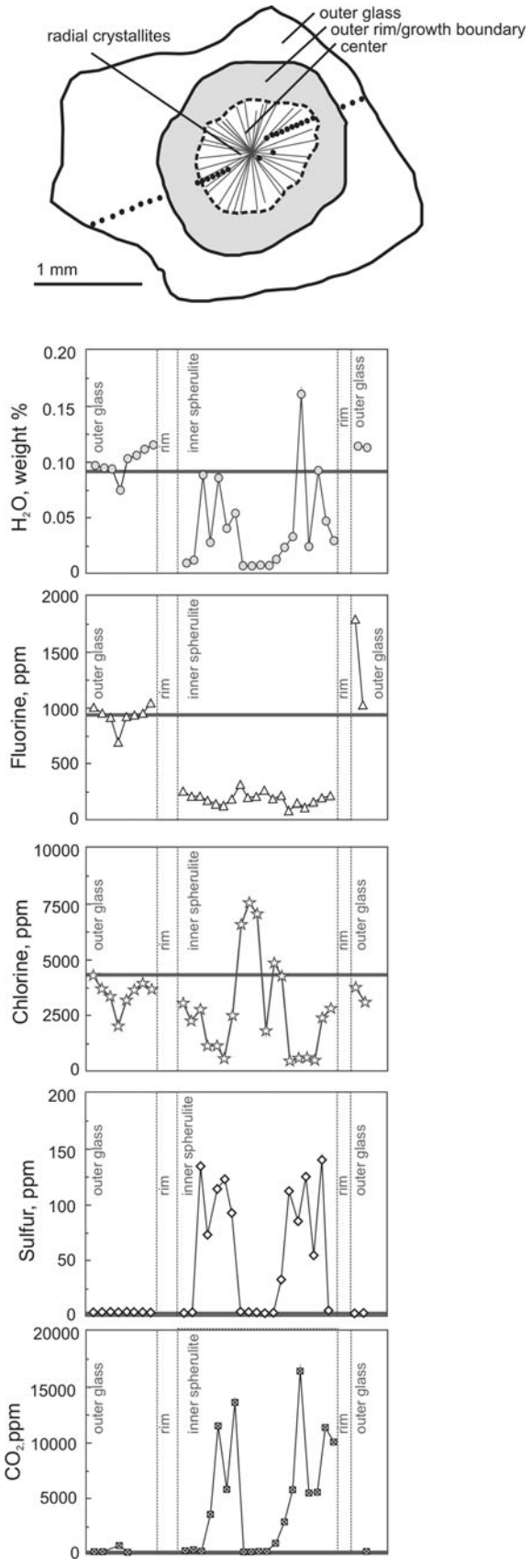

◄ **Fig. 7** Volatile (H_2O, CO_2, F, Cl and S) distribution across sample LIP-02 spherulite transect (refer to section "SIMS results: volatiles"). All concentrations are given in ppm with the exception of H_2O which is given in wt %. The horizontal line in each panel is representative of the average bulk volatile composition of the glass ($n = 30$)

However, as described above XRD analysis of spherulite material indicates that the crystallites dominantly comprise alkali feldspars (orthoclase) and cristobalite (see section "Sample petrography" and Fig. 4).

There is variation in major and minor oxides between individual profiles, but several common features can be identified: (1) low measured oxide totals (<95 %) in the crystallite boundary between the glass and inner spherulite material (Fig. 6; denoted by dashed boundaries, analyses with low totals have been removed); (2) general increase in SiO_2 in the inner spherulite from the glass/rim boundary (Fig. 6a,b, d); (3) general decrease in minor oxides such as FeO, CaO, MgO and MnO from the glass/rim boundary to the bulk glass (e.g., Fig. 6b); and (4) consistent major-oxide analyses in the glass and observable scatter in the minor-oxide analyses for crystallites and inner portions of spherulite (Fig. 6a–e). There is minimal variation in major oxides in the glass, with considerably less consistency in the inner spherulite region. Minor oxides show more pronounced variation in the glass leading up to the spherulite boundary, as shown in Fig. 6d, where concentrations of FeO and CaO decrease toward the spherulite edge. Spherulites are generally enriched in SiO_2 relative to the bulk glass and typically depleted in FeO, CaO, MgO and MnO. Enrichment of alkalis, particularly K_2O, in the glass phase is not observed as documented by other studies for heavily devitrified spherulitic glass (cf. Ewart 1971).

SIMS results: volatiles

Volatile concentrations are reported in Table 3. The compositional variation in volatile contents measured with the NanoSIMS across a glass/rim/spherulite boundary transect is shown in Fig. 7 (the average bulk volatile contents measured in the glass are denoted by the horizontal gray line). Water contents in the outer glass are slightly elevated above the average bulk composition of the glass (0.089 ± 0.012 wt%, Table 3) and increase toward the rim of the spherulite. Water concentrations inside the heterogeneous crystalline material show considerable variation and are dominantly below the "bulk" H_2O content in the glass (see section "Behavior and diffusive loss of volatiles" for discussion). Carbon dioxide is consistently below detection in the bulk glass ($\sim$12 ppm). Two spikes in CO_2 concentration are observed within the central spherulite region (Fig. 7) with a concentration low in the center, coinciding with a drop in S concentration and H_2O, yet a sharp increase in Cl and a small increase in F. This

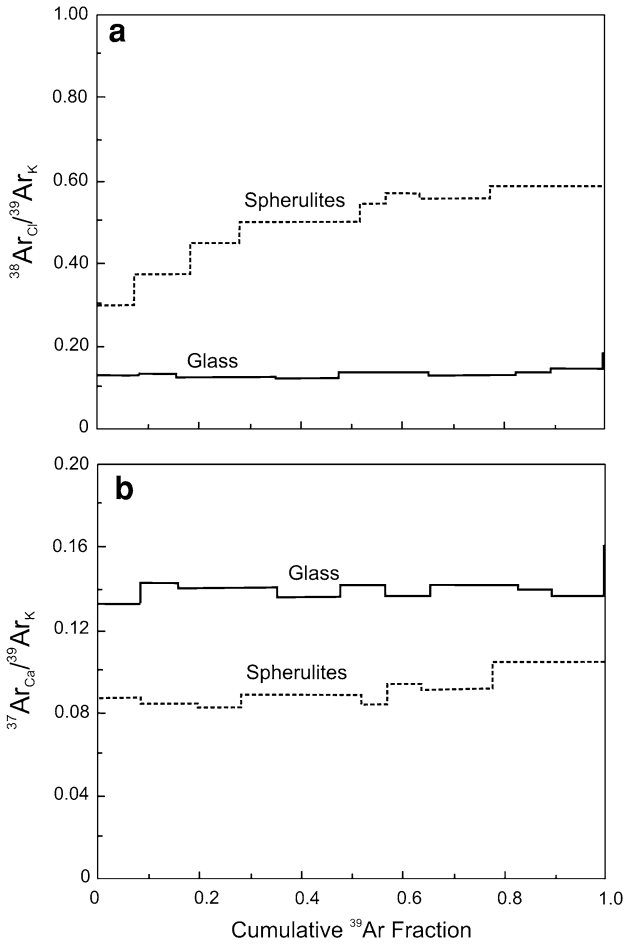

Fig. 8 $^{38}Ar_{Cl}/^{39}Ar_K$ and $^{37}Ar_{Ca}/^{39}Ar_K$ versus cumulative ^{39}Ar release in sample LIP-02 glass (**a**) and spherulite splits (**b**) (refer to section "Ar–Ar results" for discussion and Electronic Supplement 4 for full data set)

indicates the presence of compositionally heterogeneous material in the innermost portion of the spherulite, consistent with petrographic observations and EMP analyses. The general behavior of H_2O, F and Cl is similar in the glass up to the rim of the spherulite edge. From the spherulite profile edge, H_2O, CO_2 and S show an increase and then a sharp decrease to a central low point. Concentrations rise again but trend with an overall decrease to meet the rim of the spherulite, where concentrations drop well below their respective concentrations in the bulk glass. Fluorine and Cl show similar behavior across the profile, with average bulk volatile compositions below the concentrations in the glass surrounding the spherulite with the lowest concentrations present in the inner spherulite except for a central concentration "spike." Typically, Cl (4,100 ± 330 ppm) is a factor of 4 times more abundant in the bulk glass than F (950 ± 40 ppm). Sulfur is consistently below detection (~5 ppm) in the bulk glass (Fig. 7), but two concentration highs are observed in the spherulite center, corresponding to an increase in H_2O and CO_2 and a decrease in F and Cl. There is significant variability in volatile contents within the spherulite rim (e.g., the variability was so extreme for the 50 analyses in each measurement that it precluded a reliable volatile determination) and within the central crystalline spherulite region (Table 3, Fig. 7; refer to section "Behavior and diffusive loss of volatiles" for discussion).

Ar–Ar results

The results of Ar–Ar analysis are presented in Electronic Supplementary Material 4. No age information was determined due to the very young age of the samples 1230 (±40) AD (Arrighi et al. 2006); yet, the experiment yielded interesting information on Ar distribution and release patterns between the glass and crystalline spherulite material. Argon, in general, resides in the glass phase, with the spherulites containing on average a factor of 20 less ^{40}Ar. The results of $^{38}Ar_{Cl}/^{39}Ar_K$ and $^{37}Ar_{Ca}/^{39}Ar_K$ release with cumulative ^{39}Ar are shown in Fig. 8. The obsidian shows a uniform release of $^{38}Ar_{Cl}/^{39}Ar_K$, indicative of release from a single, homogenous reservoir, consistent with the glass chemistry and Cl/K ratio (~0.06) from average EMP analyses of bulk glass composition (Fig. 8a). The spherulites (Fig. 8a) display a continuous increase in $^{38}Ar_{Cl}/^{39}Ar_K$ with progressive ^{39}Ar release, indicating release from at least two phases, consistent with the mineralogical documentation set out above, for example, the spherulites are composed of radiating crystals of proportions of alkali feldspar (orthoclase) and cristobalite. The increase in $^{38}Ar_{Cl}/^{39}Ar_K$ with progressive ^{39}Ar release (and thus increasing temperature) suggests release from mineral phases with higher Cl/K ratio at higher temperatures, consistent with a transition from orthoclase to cristobalite, which fuses at a higher temperature (1,713 ± 5 °C). The $^{37}Ar_{Ca}/^{39}Ar_K$ is relatively uniform for both glass and spherulites (Fig. 8b) with cumulative ^{39}Ar release, though the ratio is higher in the glass than in spherulites, suggesting a single carrier.

Discussion

Textures, morphology and the role of deformation

Spherulite morphology can provide critical information about the temperatures at which they formed (Lofgren 1971b). The constituent parts of individual spherulites observed here comprise, from center to margin, and best exemplified in the BSE images of Fig. 6: (1) a central, spherical body of glassy and crystalline material in varying proportions with or without void space (Fig. 6c, d, respectively); (2) a zone of radiating crystallites (Fig. 6b); (3) a

narrow rim of crystalline material around the spherulite; and (4) the surrounding matrix material. The central zone compositionally ranges from coherent matrix glass and fine-grained crystalline material extending to the rim of the spherulite (e.g., Fig. 6c), to a more disaggregated clustered material dispersed among radiating crystallites (e.g., Fig. 6d, e; refer to section "Sample petrography"). The relative proportions (e.g., width of each zone) of each of these defined subdivisions vary significantly with each individual spherulite and throughout the spherulite chains. Major-, minor-oxide and volatile element concentrations are observed to vary systematically across these glass, crystallite and inner spherulite regions (see sections "CSD results" and "EMP results: glass and spherulite chemistry", Figs. 6, 7).

The most common texture observed is that of small (0.1–2.0 mm diameter) isolated spherulites in a glass matrix. This large number (25–30 spherulites per cm^2) of relatively small spherulites has traditionally been interpreted to indicate a fast rate of nucleation and a slow growth rate (Lofgren 1971a). A high nucleation rate and slow growth rate is typically indicative of growth at low temperature, where nucleation sites are readily available and diffusivity low. However, Rocche Rosse spherulites can also be densely populated in the glass matrix ($\geq$75 vol%) forming clusters and laterally continuous trails (Fig. 2d). The complex internal structure of these clusters and trails exhibits a wide range of impingement textures, suggesting that continued growth of established spherulites may have inhibited nucleation and growth of further spherulites (Keith and Padden 1964b). Additionally, where the obsidian is nearly wholly crystalline, polygonal spherulites meet with straight boundaries and triple junctions that show apparent (2D) dihedral angles approaching 120°. This latter observation suggests that in places, the obsidian flow was capable of devitrifying and thermally equilibrating under sub-solidus conditions (Hunter 1987). Thus, we recognize that though we have selected spherulites that are isolated in their fresh glass obsidian groundmass for both CSD and EMP analyses, our data must be placed in the context of continued (lower temperature) spherulite modification and devitrification, in parts of the flow.

It is important to also consider the link between spherulite formation and structural deformation of the obsidian lava flow, as reflected in the field observations and thin-section petrography. We consider it likely that much of this deformation is the result of emplacement-related flow. The rheological (i.e., highly viscous) properties of flowing rhyolitic lava make it likely that the kinematics of this flow regime are partly preserved in the structures imparted to the rocks. This is in contrast to basalt lava flows, for example, which exhibit more Newtonian-style fluid dynamics and may preserve little or no "memory" of emplacement-related flow. The notably higher concentrations of spherulites in some "flow bands" (in which the microlites are also contained; Figs. 2h, 3b) are indicative of preferential growth of spherulites in these flow bands as documented by Seaman et al. (2009). This feature suggests that the spherulites were capable of nucleating and growing while the lava flow was still mobile. Spherulites in such bands may be deformed in the plane of the banding, but are more frequently completely unaffected (Fig. 3c, d). Conversely, the microlite-defined foliation gently wraps spherulites in several instances (Fig. 3h), indicating that in some localities, spherulites were present before the final stages of foliation formation. Indeed, the mimetic growth of some spherulite rims along the foliation within flow bands suggests that spherulite growth may have continued after deformation had ceased (Fig. 2i). The growth and concentration of spherulites into flow banding therefore occurred after eruption, during slow cooling and deformation of the flow, which could have ensued for weeks based on cooling rates (Gottsmann and Dingwell 2001). The latter workers modeled the cooling history of the Rocche Rosse obsidian flow and determined that the late stage of deformation of the obsidian flow was largely controlled by cooling rates of tens of degrees K per day. They proposed that at such rates of cooling, the obsidian flow could actively deform for weeks after emplacement. Slow and sustained deformation of the cooling and advancing flow could be important to spherulite nucleation and growth in the Rocche Rosse obsidian, as is also suggested by the preserved textures. Thus, the textural evidence observed here suggests that spherulite growth was a protracted down-temperature phenomenon, closely tied in some localities to the high degree of deformation experienced by the flow.

The presence of spherulite-rich bands in the Rocche Rosse obsidian, alternating with thicker bands of more glass-rich material containing only isolated spherulites, might indicate the importance of pervasive localized microshear zones in accommodating flow-related deformation (Fig. 2c). This is supported by the observation of centimeter-to-meter scale displacements across some of these bands (see above). We suggest that the Rocche Rosse obsidian behaved as a non-Newtonian fluid during emplacement (e.g., Binghamian behavior). Bingham fluids behave viscoplastically, that is, as a solid at low stresses but as a viscous fluid once a critical yield stress has been overcome (Twiss and Moores 2007). We speculate that high-strain zones in the mobile (deforming) flow may have been more susceptible to spherulite growth as a result of this Binghamian fluid behavior. It is beyond the scope of this study to carry out a more detailed evaluation of the link between deformation and spherulite formation. We emphasize that for the textural and compositional analyses carried out here, we have carefully chosen undeformed

spherulites in fresh (glassy) layers of obsidian *between* flow bands, so that we can qualitatively rule out the effects of significant deformation on their formation. However, we also note that locally, at lower temperatures or in zones of enhanced strain, as suggested above, deformation may have played a far more significant role.

Behavior and diffusive loss of volatiles

Water, S and CO_2 typically vary conversely to Cl and F in the "inner spherulite" region, decreasing where Cl and F increase. Carbon dioxide and S are generally below detection in the bulk glass which is typical for rhyolite compositions (e.g., compared to ~30 ppm typically measured in rhyolite glass; Blank and Brooker 1994). Therefore, the high concentrations of CO_2 and S in the inner spherulite region could be suggestive of heterogeneous spherulite nucleation on compositional inhomogeneities, such as relatively S- and C-rich inclusions (e.g., wall-rock or mafic enclave material) present in the melt. Additional evidence for nucleation on inclusions exists in the major-oxide data (Table 2, Fig. 6) where occurrences of spikes in Ca concentration in the central portion of spherulites (Fig. 6e) might indicate the presence of feldspar crystals derived from disrupted and disaggregated mafic enclaves or wall rock entrained in the advancing obsidian flow (Daví et al. 2009). Indeed, small K-feldspar microlites and phenocrysts are commonly observed in thin section (e.g., Fig. 2j), showing that they serve as nucleation sites in at least some instances. Water, F and Cl profiles show decreasing concentrations from the rim edge into the glass away from the crystalline material. For instance, H_2O decreases from ~0.13 wt% to ~0.09 wt%, Cl from ~3,000 ppm to ~2,400 ppm and F from ~1,100 ppm to ~600 ppm. Note though that both Cl and F reach a central low concentration ~0.5 mm away from the spherulite edge before increasing again. These profiles are consistent with diffusive loss or expulsion of volatiles with progressive formation of anhydrous minerals within the spherulite (Keith and Padden 1963; 1964a, b; Lofgren 1971b; Meakin and Jamtveit 2010). Keith and Padden (1964b) proposed that diffusive redistribution of rejected impurities (whether by fractionation processes or due to simple structural incompatibility) drives spherulite formation in melt. They also suggested that these "impurities" are able to travel significant distances from the advancing spherulite despite the high viscosity. However, while Keith and Padden (1964a, b) purport that the rejection of impurities will have an overall slowing of spherulite growth rate, we propose an alternative model here, largely due to the fact that the main rejected structural "impurity" is H_2O. We suggest this localized loss of H_2O could form a thin H_2O-poor melt "film" immediately around the spherulite, advancing ahead of the anhydrous mineral phases (crystallites) in the spherulite. The crystallite growth front therefore "trails" (and is driven by) volatile loss from this film of melt and volatile concentration in the surrounding host rhyolite. This is particularly significant because (1) the release of H_2O away from the crystals and into the melt will lower viscosity (and thus activation energy) by depolymerization (Mysen 1976) and (2) the release of H_2O will enhance the diffusivity of numerous elements in the melt; thus, they become more readily available for spherulite crystallization. Overall, the progressive loss of volatiles away from a spherulite nucleus will trigger the localized undercooling required to drive spherulite growth, for as long as crystallite growth keeps pace with volatile expulsion. Most spherulites observed in this study have thin rims of crystalline material distinct from that comprising the bulk of the spherulite (e.g., Fig. 2f, h, section "Sample petrography") which we interpret to represent the solid-state manifestation of these H_2O-poor melt films. Below, we consider this diffusive loss or expulsion of volatiles over timescales and temperatures relevant to spherulite formation.

In order to assess the measured volatile profiles in terms of temperature and timescales of spherulite formation, we modeled the fractional loss of volatiles during high-temperature (≥800 °C) primary spherulite crystallization for the Roche Rosse obsidian. Additionally, diffusion profiles were used to evaluate volatile mobility during low-temperature ($\leq T_g$ 300–620 °C) re-crystallization of spherulites (Fig. 9). Fractional loss (represented by f) of volatiles from rhyolite melt was calculated for a spherical geometry at 300 °C and 800 °C from a duration of 1 day to 1 million years (t) using the following equation:

$$f = 1 - \left(\frac{6}{\pi^2}\right) \cdot \sum_{n=1}^{1000} \left(\frac{1}{n^2}\right) \cdot \exp\left(\frac{-Dt \cdot n^2 \cdot \pi^2}{a^2}\right)$$

(McDougall and Harrison 1999). Diffusion parameters are given in the caption to Fig. 9. Based on the diffusivity of the major volatile species at "low" (300 °C) and "high" (800 °C) spherulite crystallization temperatures, loss of volatiles is too slow for the low-temperature end-member to reproduce the measured volatile transect across spherulites in the Rocche Rosse obsidian over timescales of years up to hundreds of thousands of years (dependent upon the volatile species; refer to Fig. 9). Full retention of remaining F, Cl and S and 50 % retention of CO_2 might be preserved if nucleation and growth occurred *exclusively* as a low-temperature process. The modeled high-temperature domain, however, results in more realistic volatile loss patterns in months to years, consistent with our observations of volatile gradients across the spherulite–glass interface and with bulk glass measurements. This loss

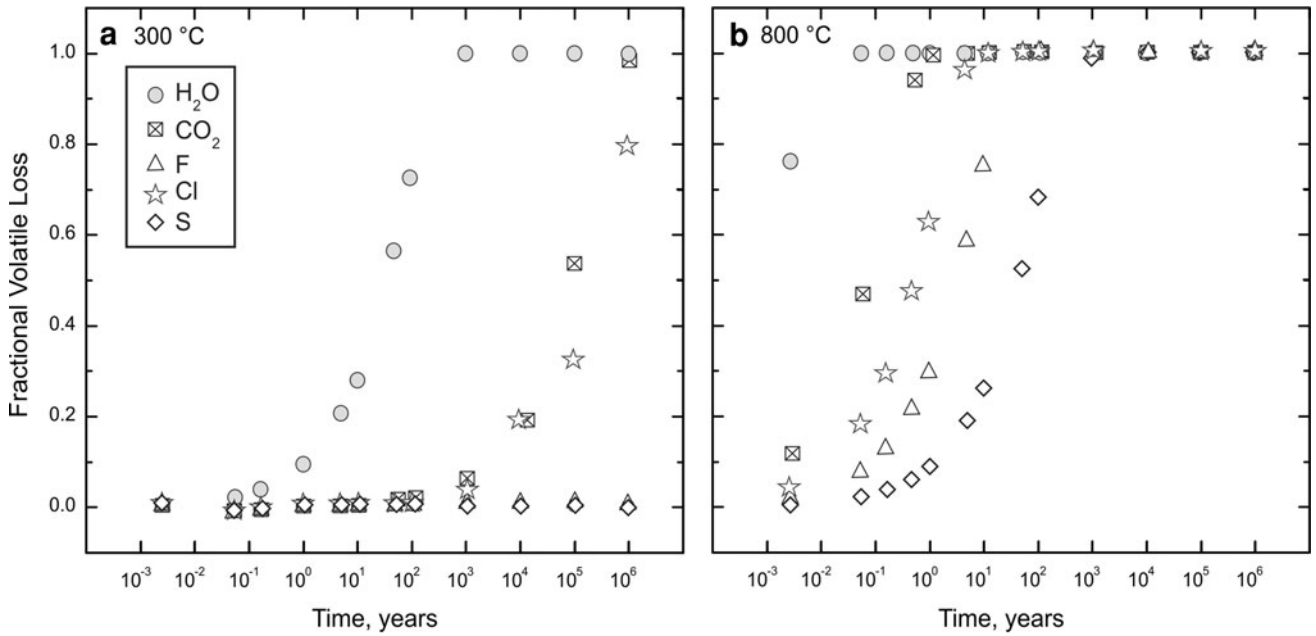

Fig. 9 **a** Modeled fractional loss of H_2O, CO_2, F, Cl and S at 300 °C and (**b**) 800 °C for the Roche Rosse obsidian. Diffusion parameters: H_2O, $D_0 = 4.6 \times 10^{-7}$ m^2s^{-1} and $E_a = 103 \pm 50$ kJ mol^{-1} (Zhang et al. 1991) for rhyolite melts containing 1–3 wt % H_2O; CO_2, $D_0 = 6.2 \times 10^{-7}$ m^2s^{-1} and $E_a = 144.6$ kJ mol^{-1} (Blank et al. 1993) for anhydrous granitic melt; F, $D_0 = 3.4 \times 10^{-5}$ m^2s^{-1} and $E_a = 215 \pm 29.5$ kJ mol^{-1} (Balcone-Boissard et al. 2009) for anhydrous phonolite melts; Cl $D_0 = 2.3 \times 10^{-8}$ m^2s^{-1} and $E_a = 134 \pm 33.1$ kJ mol^{-1} (Balcone-Boissard et al. 2009) for anhydrous phonolite melts; and S, $D_0 = 5.0 \times 10^{-6}$ m^2s^{-1} and $E_a = 221 \pm 80$ kJ mol^{-1} (Baker and Rutherford 1996) for anhydrous rhyolite melts

would be further facilitated by the increased availability of H_2O in the rhyolite melt immediately around the advancing spherulite rim resulting in localized melt depolymerization.

The characteristic diffusion distance was calculated using diffusion parameters (see Fig. 9 caption) for each volatile species over 1 year (Fig. 10). Diffusion was considered in the context of high-T spherulite crystallization (800 °C), just below the T_g range (550 °C) and low-T spherulite re-crystallization in the solid state (300 °C). These temperatures were chosen from specific ranges: (1) a high-temperature end-member within the typical rhyolite emplacement temperature range (~790–825 °C; Carmichael et al. 1974); (2) a midtemperature just below the T_g range for rhyolite (750–620 °C; Watkins et al. 2009; Fig. 10) but between the estimated temperatures for "primary" magmatic growth and the "secondary" devitrification of spherulites; and (3) a very low-temperature end-member well below T_g in the typical "devitrification" range (refer to Fig. 10). The chosen T_g range encompasses the calculated range for the Rocche Rosse obsidian flow by Gottsmann and Dingwell (2001) in their calorimetric study of cooling rates (676–706 °C). The characteristic diffusion distance for all measured volatiles ranges from large (10^5 μm; CO_2) to small (100 μm; S) at temperatures above T_g. All elements effectively plateau above and through T_g and drop off moderately below T_g, with the exception of H_2O and CO_2 which remain within a factor of 10–20 over the modeled temperature range. At temperatures below T_g, consistent with low-T devitrification and sub-solidus modification processes, the diffusion distance becomes prohibitively small (e.g., 1 μm for Ar, F and <0.1 μm for S, Cl). This is inconsistent with the measured volatile profiles and the Ar experiments (section "Argon behavior and distribution"), where volatiles would be diffusing from the spherulite growth front into the surrounding melt (on the order of 10's-100's μm).

Using the diffusivity of H_2O in a rhyolite melt/glass (here D_o and E_a are assumed constant across T_g) and the above model for spherulite formation, the timescales of spherulite crystallization in the Rocche Rosse obsidian flow can be estimated using the temperature of formation and distance travelled (radius of the spherulite and length of H_2O profile from the spherulite edge into the glass). For a typical distance of 1 mm (see Fig. 10) over the specified range of model temperatures, the timescales of crystallization vary from 4 days to 400 years based on the diffusion of H_2O.

Argon behavior and distribution

The distribution of ^{40}Ar between glass and spherulites is heavily partitioned into the glass (Fig. 8) by a factor of 20 for equivalent sample mass. The spherulites are composed of varying proportions of cristobalite, SiO_2-rich glass and

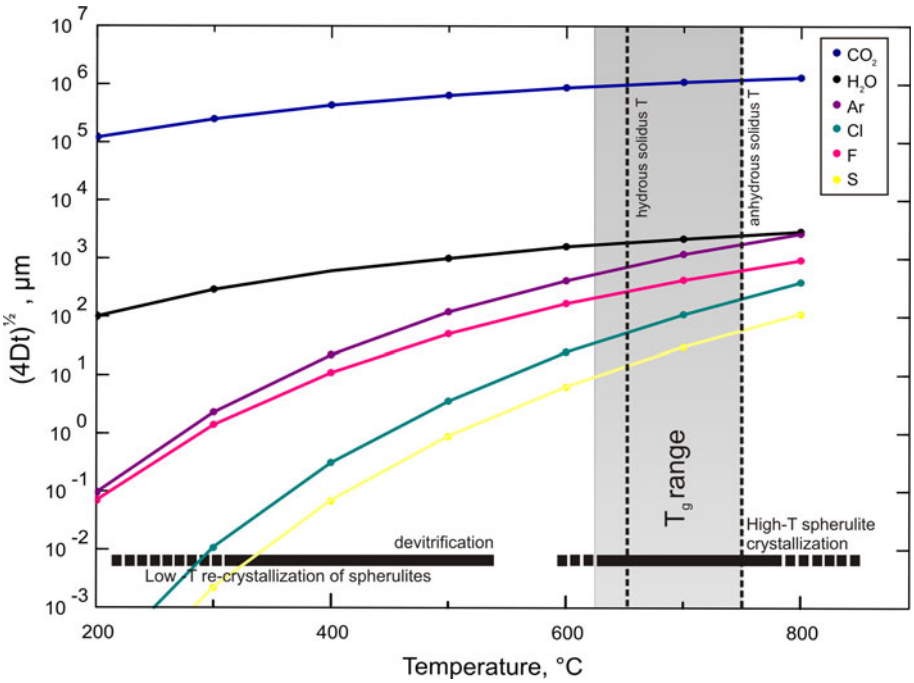

Fig. 10 Characteristic diffusion distance (μm) for each volatile species over the possible temperature ranges for primary spherulite crystallization (~800 °C) through the glass transition (~750–620 °C) and solid-state modification (~200–400 °C) over a 1-year time period. Parameters are the same as used in the fractional loss calculations and are given in the caption to Fig. 9. Argon diffusion parameters are taken from Carroll (1991)

K-feldspar. In the case of cristobalite and K-feldspar, both have a high capacity for Ar uptake and storage, particularly in the uppermost 100 s of nm to 1 μm of the mineral surface region (Watson and Cherniak 2003; Clay et al. 2010, for α and β quartz). If the formation of spherulites occurred by primary crystallization from melt as a high-temperature process, it might be expected that the cristobalite and K-feldspar would show some evidence of this in the form of elevated Ar concentrations through uptake from the melt at high temperature. Argon present in the quartz and feldspar spherulites supports formation of spherulites at high temperatures, with the Ar residing in this material representative of diffusive uptake from the melt upon crystallization over short timescales. Other studies have previously documented such high concentrations of Ar sequestered into obsidian for other potassic volcanic systems (*cf.* Clay et al. 2011).

The $^{40}Ar/^{36}Ar$ ratios observed in the crystalline material are similar to those preserved in the glass (average of 372 ± 40 and 359 ± 30 for glass and spherulites, respectively), elevated above that of air ($^{40}Ar/^{36}Ar$ = 298.56 ± 0.31; Lee et al. 2006), which would not be expected from K-free cristobalite and SiO_2-rich glass. This may indicate uptake of Ar from the surrounding groundmass in which the spherulites are situated. Additionally, the presence of expelled H_2O in the growth front rimming the spherulites enhances Ar mobility (Zhang et al. 1991; Watson 1994), creating potential for local "highways" where Ar diffuses more rapidly from the melt into growing crystal interface (refer to section "Behavior and diffusive loss of volatiles").

Spherulite formation

Assessment of hydration

Rhyolite lavas typically erupt containing 0.1–0.3 wt% H_2O, thus erupting undersaturated with respect to H_2O when compared to the atmosphere (Silver et al. 1990). This can lead to post-eruptive hydration of the glass from adsorption of atmospheric H_2O with time (Anovitz et al. 2006). This surface-adsorbed H_2O will diffuse at a rate equivalent to $k(t)^{1/2}$, producing a hydrated layer of given thickness at the glass–surface interface, which is a function of the hydration rate, k, at a specified temperature and time, t (Lofgren 1971b; Friedman and Long 1984). Contemporaneous with this diffusion of H_2O into the glass is the diffusion of alkalis, Ca and Mg out of the glass structure as a result of the hydration process. Using a hydration rate consistent with temperatures at surface conditions (4.5–11 μm^2 1,000 $years^{-1}$ for 20–30 °C; Friedman and Long 1984), we would expect a minimum hydration front of 6.3–15.4 μm^2 thickness, easily observable by optical and SEM characterization. In the Rocche Rosse obsidian, we do not observe any direct petrographic or SEM evidence for pervasive hydration. Consistent bulk H_2O contents in the glass from randomly selected points in multiple glass fragments suggest homogenous distribution of H_2O at a concentration of 0.089 wt% (Table 3), consistent with degassed, quenched rhyolite at surface conditions (Silver et al. 1990). Additionally, we do not see any evidence for alkali loss typically observed in other hydrated or altered glasses (Clay et al. 2011). We therefore rule out

widespread and *systematic* hydration of the glass during eruption and emplacement, though we recognize that hydration on a local scale controlled by the local structure of the obsidian flow could be important to spherulite growth.

Assessment of devitrification and low-temperature re-crystallization

Devitrification and re-crystallization is highly dependent upon emplacement temperature, cooling rate and glass H_2O content. Devitrification of rhyolite glass will occur relatively rapidly at elevated temperature and H_2O contents (activation energy of viscosity, $E_a = 45$ kcal/mol at 1.5 wt% H_2O), but rather slowly at surface temperature and low H_2O contents ($E_a = 80$ kcal mol at 0.3 wt% H_2O; Friedman and Long 1984). At low temperatures (below T_g) in unhydrated obsidian (<0.3 wt% H_2O), crystallization is prohibitively slow due to the high activation energy of viscosity at surface conditions (e.g., diffusion through a highly polymerized melt is restricted). Considering the young age of the Rocche Rosse obsidian, widespread hydration and emplacement temperatures above the solidus would be required to produce the observed spherulitic textures through devitrification over the given time since eruption. The lack of observed hydration supports the notion that *the onset* of spherulite formation had to occur above T_g. We propose that the spherulite crystallization process in the Rocche Rosse obsidian ensued from a high-temperature state (≤800 °C), as "primary" crystallization in a rhyolite body upon emplacement and ensued with cooling of the flow as a "continuum" of spherulite crystallization and growth. However, we also suggest that the polygonal spherulitic textures observed in some highly crystalline samples indicate continued modification of the spherulitic textures during lower temperature sub-solidus maturation. In addition, the preferential occurrence of crystalline material in the hinges of some large folds, which likely formed in the sub-solidus, also points toward devitrification. These observations suggest that while devitrification may not have been the dominant process in spherulite formation, it was capable of locally modifying spherulite textures in the Rocche Rosse obsidian. Additionally, the presence of reddish rims observed as overgrowths on some spherulite edges [Fig. 2g; also observed in the study of Castro et al. (2009)] could be the result of late-stage formation reflecting a change in oxidation state.

Application of CSD to the quantitative analysis of spherulitic texture

The rate of isothermal spherulitic crystallization has been shown to be linear (i.e., growth at a constant rate) despite being a highly non-equilibrium crystallization process. Keith and Padden (1964b) proposed a deviation from the linearity of growth rate when high concentrations of "impurities" are rejected from the growing spherulite, effectively slowing the growth rate. However, in the case of the spherulites from the Rocche Rosse obsidian flow, the rejected impurity is largely H_2O, sequestered in the melt around the spherulites and therefore, perhaps, contributing to spherulite growth. Given that spherulite growth would be linear within each defined growth stage (see below), the use of CSDs as a tool for interpretation of spherulitic textures may be effective. It should be noted that Castro et al. (2008) pointed out that CSD analysis might not work well for spherulite texture, given their conclusion that spherulites exhibit size-dependent growth. However, CSD analysis has been applied to numerous systems in which textural coarsening (e.g., Ostwald ripening; see Higgins 2010 for a review) occurs, and comparison of CSDs from multiple, genetically related samples may still provide useful, albeit qualitative, information, as shown here. Indeed, the similarities in CSD plot shapes are emphasized by the pronounced, single trends shown by CSD parameters (Characteristic Length, Volume Phase Proportion and Intercept, Table 1), indicating that there is no evidence, at least within the sample set measured, for more than one continuum of spherulite nucleation and growth.

Model of spherulite formation in the Rocche Rosse obsidian

Spherulites are common in a variety of natural materials (e.g., multi-component melt, plastics, metals, etc.), with a diverse array of physical and chemical properties. Experimental spherulitic crystallization has also been shown to be similar in entirely dissimilar materials (Keith and Padden 1963, 1964a, b; Meakin and Jamtveit 2010). This strongly suggests a common mechanism of spherulite nucleation and growth over a wide range of physical and chemical properties. Our CSD data qualitatively support this idea, as samples with visually different textures from apparently unrelated parts of the Rocche Rosse lava flow have unexpectedly similar CSD plot shapes and slopes. However, growth and formation of spherulitic textures from a multi-component melt is a complex process and a function of two competing factors: the rate of nucleation (which decreases with increasing temperature) and the rate of crystal growth (which increases with increasing temperature) (Keith and Padden 1964b). Thus, a maximum in the development of spherulitic textures would be expected at a temperature where these two factors are essentially equivalent. Here we discuss the conditions for the growth of the spherulites in the Rocche Rosse obsidian flow in the context of these factors. We suggest that the observed spherulitic textures in

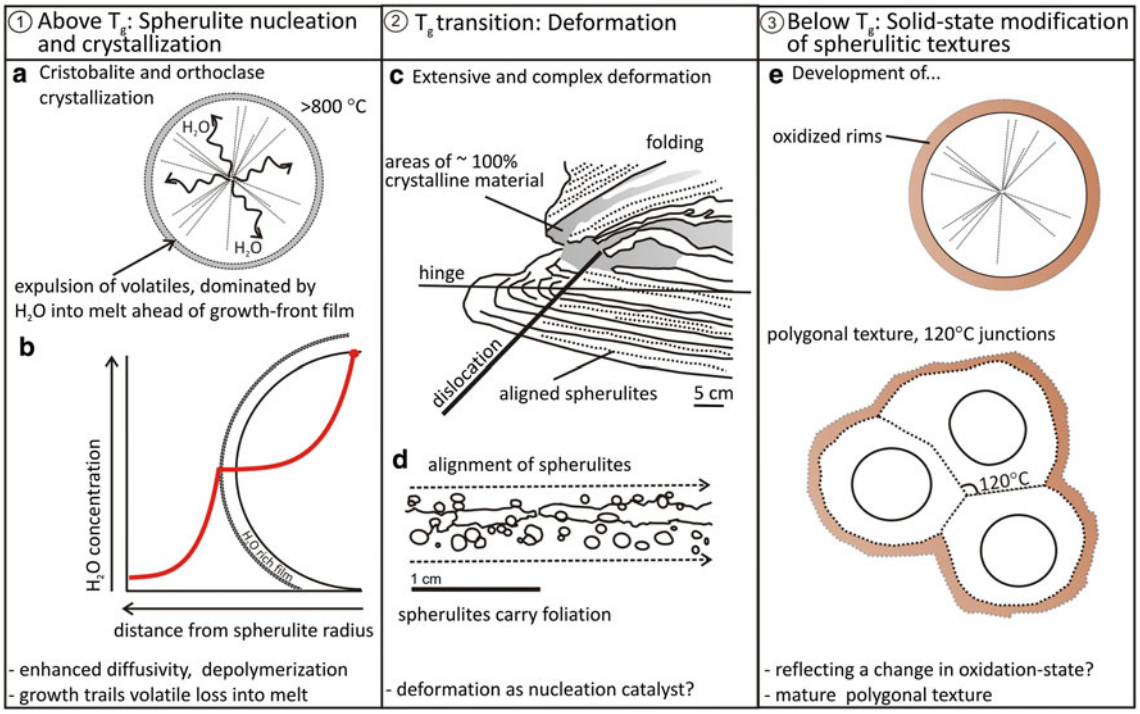

Fig. 11 Schematic of temperature continuum growth model for the spherulites in the Rocche Rosse obsidian. (*1*) Above T_g spherulite nucleation and crystallization dominates. **a** Volatiles, dominantly water, are expelled into a thin melt film surrounding the growing spherulite with crystallization of anhydrous phases, in this case cristobalite and alkali feldspar (orthoclase). **b** Water decreases from the inner spherulite to the melt film, where water is concentrated as it is expelled. Concentration of water drops off from the melt film into the surrounding melt. (*2*) Through the T_g temperature range, deformation ensues, potentially acting as a catalyst for future nucleation points and forms the dominant spherulite fabric (**c**). **d** Spherulites align and record this deformation. Folding is complex. (*3*) Evidence for solid-state modification (below T_g) of existing spherulite textures exists in the form of "honeycombed" (polygonal) textures with well-developed triple junctions (particularly in heavily crystalline areas). Changes in Fe-oxidation state are observed with reddish-brown rims surrounding some spherulites (**e**)

the Rocche Rosse obsidian favor a continuum of spherulite formation over a broad range of temperatures, starting from rhyolite emplacement temperatures (~790–825 °C; Carmichael et al. 1974) through T_g (750–620 °C; Swanson et al. 1989; Watkins et al. 2009), and propose the following model for a down-temperature continuum of spherulite growth in the Rocche Rosse obsidian (Fig. 11):

1. Eruption and rapid cooling of rhyolite magma is followed by downslope transport of the obsidian flow. An initial period of growth at magmatic temperatures (≥790–825 °C) is dominated by slow nucleation and fast crystal growth. Spherulites nucleate and grow during this stage, fueled by expulsion of impurities, such as H_2O, from a thin melt film surrounding the spherulites and enhancing growth locally through increased diffusivity and depolymerization in the melt around the spherulite and attendant H_2O-poor rim (Fig. 11a, b). These spherulites are largely in place prior to deformation and may be subsequently aligned in flow fabrics or, more rarely, flattened and/or stretched as shown in Fig. 3c, d.
2. At intermediate temperatures (<800 °C and through T_g) the lava flow is progressively cooled and intense deformation ensues, resulting first in the development of the penetrative microlite foliation as the viscosity increases. We hypothesize that this deformation phase extends through the T_g range. This is supported by textural evidence, such as the alignment of microlites within a strong penetrative foliation that is defined by the spherulite bands (Fig. 2h) and which occasionally subtly wraps spherulites (Fig. 2j). Syn-deformation processes potentially induce further spherulite nucleation by providing new nucleation sites, where spherulites are focused and concentrated into regions of high strain (Fig. 2a, i).
3. Continued emplacement-related deformation results in the development of larger-scale structures, such as complex small- and large-scale folding (Figs. 3a, b, 11c, d). In some particularly high-strain regions, spherulites develop into layers of nearly completely crystalline material, forming dense bands such that individual spherulites are no longer distinguishable from one another (Figs. 2d, 3b). The last stages of

deformation cause some fabrics to gently wrap and/or drape isolated spherulites and result in small fractures around the spherulites (Fig. 2h). A low-temperature (≤650 °C) growth stage ensues where nucleation is favored over crystal growth, resulting in numerous nucleation sites, but small spherulites.

4. At progressively low temperature (300 °C), the crystalline material is subjected to continued devitrification, manifested by solid-state modification and recrystallization of spherulites, resulting in the 120° dihedral angles observed (Figs. 2g, 11e) and polygonal "honeycombed" textures (Fig. 2k). Reddish rims form around some spherulites (Figs. 2g, 11e) with oxidation (Castro et al. 2009). This low-temperature process is evidenced by the overall textural maturation and combination of individual spherulites into several millimeter-thick blocks of crystalline material. Here, the proportion of fresh glass preserved in the section is typically less than 10 % of the total rock. We suggest that these textures represent the latest stage sub-solidus, modification and textural equilibration of the most crystalline regions of the spherulitic Rocche Rosse obsidian.

Conclusion

We envisage a continuum of spherulite formation in the Rocche Rosse obsidian flow, beginning above T_g as the product of primary crystallization and the result of a high degree of undercooling ($\Delta T \sim$ 100–250 °C). The growth of spherulite-forming crystallites occurs into a H_2O-poor melt film that is locally surrounded in turn by melt enriched in H_2O. Crystallite growth responds to localized undercooling of this thin volatile-poor film, itself formed through volatile expulsion into the surrounding rhyolite. The enrichment of the rhyolite melt around spherulites in H_2O is important for enhanced depolymerization of the melt and may contribute toward enhanced volatile diffusion, aiding volatile mobility in the melt and making available components required for crystallization on a rapid timescale (days). Spherulite crystallization continues as a down-temperature growth continuum, balanced by nucleation versus growth rate. The spherulites experience sub-solidus textural modification and equilibration below T_g both syn- and post-deformation. Additionally, the role of deformation may be important in providing further nucleation sites that act as catalysts for spherulite growth. The timescale of spherulite formation in the Rocche Rosse is estimated at ~4 days at high temperatures (≥800 °C) but with further spherulite modification over longer timescales (up to 400 years at low temperatures; ≤300 °C).

Acknowledgments The authors gratefully acknowledge Andy Tindle (The Open University) for assistance with electron microprobe analyses. Erik Hauri and Julie O'Leary are thanked for generously sharing their knowledge of volatile measurements in glass and standard materials. Christelle Guillermier and Ian Franchi (The Open University) are thanked for NanoSIMS measurement assistance. Richard Darton (Keele University) is thanked for assistance with XRD analysis. James Schwanethal (The Open University) is gratefully acknowledged for assistance with Ar–Ar measurements and as author of the "ArMaDiLo" software used for data reduction. We appreciate the comments of Thomas Monecke and two anonymous reviewers, as well as the editorial handling of Jochen Hoefs, which greatly improved the manuscript. PC acknowledges support from an Open University studentship and a CEPSAR grant for interdisciplinary research awarded to PC and HB.

References

Anderson HJ, Jackson JA (1987) The deep seismicity of the Tyrrhenian Sea. Geophys J R Astron Soc 91:613–637

Anovitz LM, Riciputi LR, Cole DR, Fayek M, Elam JM (2006) Obsidian hydration: a new paleothermometer. Geology 34:517–520

Arrighi S, Tanguy J, Rosi M (2006) Eruptions of the last 2200 years at Vulcano and Vulcanello (Aeolian Islands, Italy) dated by high-accuracy archeomagnetism. Phys Earth Planet Inter 159:225–233

Baker DR, Freda C (2001) Eutectic crystallization in the undercooled orthoclase-quartz-H_2O system: experiments and simulations. Eur J Miner 13:453–466

Baker L, Rutherford MJ (1996) Sulfur diffusion in rhyolite melts. Contrib Miner Petrol 123:335–344

Balcone-Boissard H, Baker DR, Villemant B, Boudon G (2009) F and Cl diffusion in phonolitic melts: influence of the Na/K ratio. Chem Geol 263:89–98

Barberi F, Gasparini P, Innocenti F, Villari L (1973) Volcanism of the southern Tyrrhenian Sea and its geodynamic implications. J Geophys Res 78:5221–5232

Beccaluva L, Rossi PL, Serri G (1982) Neogene to recent volcanism of the southern Tyrrhenian–Sicilian area: implications for the geodynamic evolution of the Calabrian Arc. Earth Evol Sci 3:222–238

Best MG (2003) Igneous and metamorphic petrology. Blackwell, Oxford, p 729

Bigazzi G, Bonadonna FP (1973) Fission track dating off the obsidian of Lipari Island (Italy). Nature 242:322–323

Blank JG, Brooker RA (1994) Experimental studies of carbon dioxide in silicate melts: solubility, speciation, and stable carbon isotope behaviour. In: Carroll MR, Holloway JR (eds) Volatiles in Magmas, Rev Miner vol 30, pp 157–182

Blank JG, Stolper EM, Carroll MR (1993) Solubilities of carbon dioxide and water in rhyolite melt at 850 °C and 750 bars. Earth Planet Sci Lett 119:27–36

Boorman S, Boudreau A, Kruger FJ (2004) The lower zone-critical zone transition of the Bushveld Complex: a quantitative textural study. J Petrol 45:1209–1235

Cabrerra A, Weinberg RF, Wright HMN, Zlotnik S, Cas RAF (2011) Melt fracturing and healing: a mechanism for degassing and origin of silicic obsidian. Geology 39:67–70

Caputo MG, Panza F, Postpischl D (1972) New evidences about the deep structure of the Lipari arc. Tectonophys 15:219–231

Carmichael I, Turner F, Verhoogen J (1974) Igneous petrology. McGraw-Hill, New York, p 739

Carroll MR (1991) Diffusion of Ar in rhyolite, orthoclase and albite composition glasses. Earth Planet Sci Lett 103:156–168
Cas RAF, Wright JV (1987) Volcanic successions: modern and ancient. Unwin Hyman, London, p 528
Castro JM, Manga M, Cashman KV (2002) Dynamics of obsidian flows inferred from microstructures: insights from microlite preferred orientations. Earth Planet Sci Lett 199:211–226
Castro JM, Beck P, Tuffen H, Nichols ARL, Dingwell DB, Martin MC (2008) Timescales of spherulite crystallization in obsidian inferred from water concentration profiles. Am Miner 93:1816–1822
Castro JM, Cottrell E, Tuffen H, Logan AV, Kelley KA (2009) Spherulite crystallization induces Fe-redox redistribution in silicic melt. Chem Geol 268:272–280
Clay PL (2010) Ar–Ar dating of young volcanic glass. PhD thesis, The Open University, pp 459
Clay PL, Baxter EF, Cherniak DJ, Kelley SP, Thomas JB, Watson EB (2010) Two diffusion pathways in quartz: a combined UV-laser and RBS study. Geochim Cosmochim Acta 74:5906–5925
Clay PL, Kelley SP, Sherlock SC, Barry TL (2011) Partitioning of excess argon between alkali feldspars and glass in a volcanic system. Chem Geol 289:12–30
Cole GAJ, Butler GW (1892) On the lithophyses in the obsidian of the Rocche Rosse, Lipari. Quart J Geol Soc 48:438–443
Cortese M, Frazzetta G, La Volpe L (1986) Volcanic history of Lipari (Aeolian Islands, Italy) during the last 10,000 years. J Volcanol Geotherm Res 27:117–133
Crisci GM, De Rosa R, Esperanca S, Mazzuoli R, Sonnino M (1991) Temporal evolution of a three component system: the island of Lipari (Aeolian Arc, southern Italy). Bull Volcanol 53:207–221
Daví M, De Rosa R, Barca D (2009) A LA-ICP-MS study of minerals in the Rocche Rosse magmatic enclaves: evidence of a mafic input triggering the latest silicic eruption of Lipari Island (Aeolian Arc, Italy). J Volcanol Geotherm Res 182:45–56
De Astis G, Ventura G, Vilardo G (2003) Geodynamic significance of the Aeolian volcanism (Southern Tyrrhenian Sea, Italy) in light of structural, seismological and geochemical data. Tectonics 22(4):1040. doi:10.1029/2003TC001506
Dellino P, La Volpe L (1995) Fragmentation versus transportation mechanism in the pyroclastic sequence of Monte Pilato-Rocche Rosse (Lipari, Italy). J Volcanol Geotherm Res 64:211–231
Duffield WA, Dalrymple GB (1990) The Taylor Creek Rhyolite of New Mexico: a rapidly emplaced field of domes and lava flows. Bull Volcanol 52:475–478
Ewart A (1971) Chemical changes accompanying spherulitic crystallization in rhyolitic lavas, Central Volcanic Region, New Zealand. Miner Mag 38:424–434
Fenn PM (1977) The nucleation and growth of alkali feldspars from hydrous melts. Can Miner 15:135–161
Fink JH (1983) Structure and emplacement of a rhyolitic obsidian flow. Little Glass Mountain Medicine Lake highland, northern California. Geol Soc Am Bull 94:362–380
Friedman I, Long W (1984) Volcanic glasses, their origin and alteration processes. J Non-Cryst Solids 67:127–133
Gasparini C, Iannaccone G, Scandone P, Scarpa R (1982) Seismotectonics of the Calabrian arc. Tectonophys 84:267–286
Gimeno D (2003) Devitrification of natural rhyolitic obsidian glasses: petrographic and microstructural study (SEM + EDS) of recent (Lipari island) and ancient (Sarrabus, SE Sardinia) samples. J Non-Cryst Solids 323:84–90
Gottsmann J, Dingwell DB (2001) The cooling of frontal flow ramps: a calorimetric study on the Rocche Rosse rhyolite flow, Lipari, Aeolian Islands, Italy. Terra Nova 13:157–164
Hauri E, Wang J, Dixon JE, King PL, Mandeville C, Newman S (2002) SIMS analysis of volatiles in silicate glasses 1. Calibration, matrix effects and comparisons with FTIR. Chem Geol 183:99–114
Higgins MD (1994) Determination of crystal morphology and size from bulk measurements on thin sections: numerical modelling. Am Miner 79:113–119
Higgins MD (2000) Measurement of crystal size distributions. Am Miner 85:1105–1116
Higgins MD (2002) Closure in crystal size distributions (CSD), verification of CSD calculations, and the significance of CSD fans. Am Miner 87:171–175
Higgins MD (2006a) Quantitative textural measurements in igneous and metamorphic petrology, 1st edn. Cambridge University Press, Cambridge, p 270
Higgins MD (2006b) Verification of ideal semi logarithmic, lognormal or fractal crystal size distributions from 2D datasets. J Volcanol Geotherm Res 154:8–16
Higgins MD (2010) Textural coarsening in igneous rocks. Intern Geol Rev 1:1–23
Hunter RH (1987) Textural equilibrium in layered igneous rocks. In: Parsons I (ed) Origins of igneous layering. Reidel, Dordrecht, pp 473–503
Jerram DA, Cheadle MJ, Philpotts AR (2003) Quantifying the building blocks of igneous rocks: are clustered crystal frameworks the foundation. J Petrol 44:2033–2051
Keith H Jr, Padden F (1963) A phenomenological theory of spherulitic crystallization. J Appl Phys 34:2409–2421
Keith H Jr, Padden F (1964a) Spherulitic crystallization from the melt. I. Fractionation and impurity segregation and their influence on crystalline morphology. J Appl Phys 35:1270–1285
Keith H Jr, Padden F (1964b) Spherulitic crystallization from the melt. II. Influence of fractionation and impurity segregation on the kinetics of crystallization. J Appl Phys 35:1286–1296
Keller J (1970) Datierung der Obsidiane und Bimstuffe von Lipari. Neues Jahrb Geol P M, pp 90–101
Keller J (1982) Mediterranean island arcs. In: Thorpe RS (ed) Andesites. Wiley, Chichester, pp 307–325
Keller J (2002) Lipari's fiery past: dating the medieval pumice eruption of Monte Pelato. International Conference "The fire between air and water", UNESCO-Regione Siciliana, Lipari, 29 September–2 October 2002
Lee J, Marti K, Severinghaus J, Kawamura K, Yoo H, Kim J (2006) A redetermination of the isotopic abundances of atmospheric argon. Geochm Cosmochim Acta 70:4507–4512
Lofgren G (1971a) Spherulitic textures in glassy and crystalline rocks. J Geophys Res 76:5635–5648
Lofgren G (1971b) Experimentally produced devitrification textures in natural rhyolitic glass. Geol Soc Am Bull 82:111–124
Lucchi F, Tranne CA, Rossi PL (2010) Stratigraphic approach to geological mapping of the late Quaternary volcanic island of Lipari, Aeolian archipelago, southern Italy. In: Groppelli G, Viereck-Goette L (eds) Stratigraphy and geology of volcanic areas. Geol Soc Am Spec Paper vol 464, pp 1–32
Ludwig KR (2003) Isoplot 3.00: A geochronologic toolkit for Microsoft Excel. Berkley Geochronology Center Special Publication No 4, pp. 70
Marsh BD (1998) On the interpretation of crystal size distributions in magmatic systems. J Petrol 39:553–599
McDougall I, Harrison TM (1999) Geochronology and thermochronology by the $^{40}Ar/^{39}Ar$ method. Oxford University Press, New York, p 269
Meakin P, Jamtveit B (2010) Geological pattern formation by growth and dissolution in aqueous systems. Proc R Soc London A 466:659–694
Monecke T, Renno AD, Herzig PM (2004) Primary clinopyroxene spherulites in basaltic lavas from the Pacific-Antarctic ridge. J Volcanol Geotherm Res 130:51–59

Mysen BO (1976) The role of volatiles in silicate melts: solubility of carbon dioxide and water in feldspar, pyroxene and feldspathoid melts to 30 kb and 1625 °C. Am J Sci 276:969–996

Ninkovich D, Hays JD (1972) Mediterranean island arcs and origin of high potash volcanoes. Earth Planet Sci Lett 16:331–345

Pichler H (1980) The island of Lipari. Ren Soc Ital Miner e Petrol 36:415–440

Renne PR, Swisher CC, Deino AL, Karner DB, Owens TL, DePaolo DJ (1998) Intercalibration of standards, absolute ages and uncertainties in $^{40}Ar/^{39}Ar$ dating. Chem Geol 145:117–152

Rust AC, Cashman KV (2007) Multiple origins of obsidian pyroclasts and implications for changes in the dynamics of the 1300 B.P. eruption of Newbury Volcano, USA. Bull Volcanol 69:825–845

Saal AE, Hauri EH, Lo Casico M, Van Orman JA, Rutherford MC, Cooper RF (2008) Volatile content of lunar volcanic glasses and the presence of water in the Moon's interior. Nature 454:192–195

Scandone P (1979) Origin of the Tyrrhenian Sea and Calabrian Arc. Boll Soc Geol It 98:27–34

Seaman SJ, Dyar MD, Marinkovic N (2009) The effects of heterogeneity in magma water concentration on the development of flow banding and spherulites in rhyolitic lava. J Volcanol Geotherm Res 183:157–169

Silver LA, Ihinger PD, Stolper E (1990) The influence of bulk composition on the speciation of water in silicate glasses. Contrib Miner Petrol 104:142–162

Smith RK, Tremallo RL, Lofgren GE (2001) Growth of megaspherulites in a rhyolitic vitrophyre. Am Miner 86:589–600

Swanson SE (1977) Relation of nucleation and crystal-growth rate to the development of granitic textures. Am Miner 62:966–978

Swanson SE, Naney MT, Westrich HR, Eichelberger JC (1989) Crystallization history of Obsidian Dome, Inyo Domes, California. Bull Volcanol 51:161–176

Tanguy J-C, Le Goff M, Principe C, Arrighi S, Chillemi V, Paiotti A, La Delfa S, Patanè G (2003) Archeomagnetic dating of Mediterranean volcanics of the last 2100 years: validity and limits. Earth Planet Sci Lett 211:111–124

Tenner TJ, Hirschmann MM, Withers AC, Hervig RL (2009) Hydrogen partitioning between nominally anhydrous upper mantle minerals and melt between 3 and 5 GPa and applications o hydrous peridotite partial melting. Chem Geol 262:42–56

Turner S, George R, Jerram DA, Carpente N, Hawkesworth C (2003) Case studies of plagioclase growth and residence times in island arc lavas from Tonga and the Lesser Antilles, and a model to reconcile discordant age information. Earth Planet Sci Lett 214:279–294

Twiss RJ, Moores EM (2007) Structural geology. W. H. Freeman and Company, New York, p 736

Watkins J, Manga M, Huber C, Martin M (2009) Diffusion-controlled spherulite growth in obsidian inferred from H_2O concentration profiles. Contrib Miner Petrol 157:163–172

Watson EB (1994) Diffusion in volatile bearing magmas In: Carroll MR, Holloway JR (eds) Volatiles in Magmas, Rev Miner vol 30, pp 371–411

Watson EB, Cherniak DJ (2003) Lattice diffusion of Ar in quartz, with constraints on Ar solubility and evidence of nanopores. Geochim Cosmochim Acta 67:2043–2062

Zhang Y, Stolper EM, Wasserburg GJ (1991) Diffusion of water in rhyolitic glasses. Geochim Cosmochim Acta 55:441–456